Post-fire Evolution of Ravel Transport Regimes in the Diablo Range, CA

Hayden L Jacobson[1], Danica L Roth[2], Gabriel Walton[1], Margaret Zimmer[3,4], Kerri Johnson,[5,6]

[1]Colorado School of Mines, Department of Geology and Geological Engineering, Golden, CO, 80401, United States
5 [2]University of Colorado Boulder, Cooperative Institute for Research in Environmental Sciences, Boulder, CO, 80309, United States
[3]University of California Santa Cruz, Department of Earth and Planetary Sciences, Santa Cruz, CA, 95064, United States
[4] Department of Soil and Environmental Sciences, University of Wisconsin, Madison, WI, 53707, United States
[5]University of California Berkeley, Department of Integrative Biology, Berkeley, CA, 94720 United States
10 [6]University of California Santa Barbara, UC Natural Reserve System, Santa Barbara, CA, 93106, United States

Correspondence to: Hayden L. Jacobson (jacobson@mines.edu)

Abstract. Post-fire changes to the transport regime of dry ravel, which describes the gravity-driven transport of individual particles downslope, are poorly constrained but critical to understand as ravel may contribute to elevated sediment fluxes and
15 associated debris-flow activity observed post-fire in the western United States. In this study, we evaluated post-fire variability in dry ravel travel distance exceedance probabilities and disentrainment rates in the Diablo Range of central coastal California following the Santa Clara Unit Lightning Complex fire of August 2020. Between March 2021 and March 2022, we conducted repeat field experiments simulating ravel with in situ particles (3–35 mm diameter) on a range of experimental surface gradients (0.38-0.81) on both grassy south-facing slopes and oak woodland north-facing slopes. We
20 characterized post-fire evolution in particle transport by fitting a probabilistic Lomax distribution model to the empirical travel distance exceedance probabilities for each experimental particle size, surface gradient, and time. The resulting Lomax shape and scale parameters were used to identify the transport regime for each subset of simulated ravel, ranging from "bounded" (light-tailed or local) to "runaway" (heavy-tailed or nonlocal) motion. Our experimental results indicated that as vegetation recovered over the first two years post-fire, the behavior of small particles (median intermediate axis of 6 mm)
25 became less similar across the experimental sites due to different vegetation structures, whereas medium and large particles (median intermediate axes of 13 mm, 28 mm) exhibited a general transition from more runaway to more bounded transport, and large particles became less sensitive to surface gradient. All particle sizes exhibited a decrease in the length scale of transport with time. Of all particle subsets, larger particles on steeper slopes were more likely to experience nonlocal transport, consistent with previous observations and theory. These findings are further corroborated by hillslope and channel
30 deposits, which suggest that large particles were preferentially evacuated from the hillslope to the channel during or immediately after the fire. Our results indicate that nonlocal transport of in situ particles likely occurs in the experimental study catchment, and the presence of wildfire increases the likelihood of nonlocal transport, particularly on steeper slopes.

1 Introduction

The average yearly areal extent of burned land in the Western United States is increasing (e.g., Parks & Abatzoglou, 2020). Fire is an effective agent of weathering and results in the mobilization of sediment, with a temporary increase in sediment transport rates frequently observed post-wildfire (e.g., Roering & Gerber, 2005; Shakesby & Doerr, 2006; Swanson, 1981; Wondzell & King, 2003). It is critical to characterize the post-fire evolution of transport mechanisms that contribute to changes in sediment transport rates, as it can inform our understanding of post-fire variability in catchment scale sediment loading and associated hazards, such as debris flows (e.g., DiBiase & Lamb, 2019; Florsheim et al., 1991; Jackson & Roering, 2009). Additionally, the form of hillslopes in steeplands is governed by the length scale of sediment transport and understanding post-fire sediment transport regimes informs the appropriate construction of long-term landscape evolution models (e.g., Gabet and Mendoza 2012; Tucker & Bradley, 2010).

A contributor to the observed post-fire increase in sediment transport in the Western U.S. is dry ravel, the rarified, gravity-driven transport of individual gravels or soil aggregates, collectively referred to here as "particles." Ravel is entrained by surface disturbances such as bioturbation or wildfire (Gabet, 2003; Jackson & Roering, 2009; Roering & Gerber, 2005). The incineration of vegetation dams during wildfires releases retained sediment on slopes greater than the angle of repose of the stored sediment, which then travels downslope as ravel (Bennett, 1982; Dibiase & Lamb, 2013). The loss of vegetation and associated surface roughness also results in reduced frictional resistance to the gravity-driven transport of ravel entrained in the months following a fire. This change may drive a transition between a distance-bounded particle motion regime defined by net kinetic energy loss via friction to a runaway motion regime defined by the conversion of gravitational potential energy to kinetic energy, resulting in net energy gain (Furbish et al., 2021a; Roth et al., 2020). On hillslopes, this transition has been observed to occur at slopes of 30-40 degrees and has often been described as a shift from local to nonlocal transport (DiBiase et al., 2017; Furbish et al., 2021b; Gabet, 2003; Gabet & Mendoza, 2012; Roering & Gerber, 2005). Nonlocal transport describes a condition in which the upslope topography influences the flux at a downslope position, as this "nonlocal" topography controls the motions of particles that are transported long distances (Foufoula-Georgiou et al., 2010; Furbish & Haff, 2010; Furbish & Roering, 2013). A theoretical transition between local and nonlocal transport can be described in terms of the form of the particle travel distance exceedance probability distribution (i.e., the complementary cumulative distribution of travel distances). As particle motion transitions from bounded (local) to runaway (nonlocal), the form of the travel distance exceedance probability distribution transitions from light-tailed to heavy-tailed (Foufoula-Georgiou et al., 2010; Gabet & Mendoza, 2012; Roth et al, 2020; Tucker and Bradley, 2010). Since the sediment flux depends on the rate of particle entrainment and the distance particles travel before disentraining, the longer particle travel distances associated with nonlocal transport are expected to result in higher sediment fluxes (e.g., DiBiase et al., 2017; Furbish & Roering, 2013).

65   Recent experimental work suggests that nonlocal transport may be more likely to occur post-fire due to the decreased probability of particle disentrainment, potentially leading to increased fluxes post-fire (DiBiase et al., 2017; Furbish et al., 2021b; Roth et al., 2020). Major increases in catchment-scale sediment yield due to ravel fluxes in the first year after fire have been well-documented in the Pacific Northwest (e.g., Jackson & Roering, 2009; Roering & Gerber, 2005; Swanson, 1981) and California (e.g., Collins & Ketcham, 2001; DiBiase & Lamb, 2013; East et al., 2021; Florsheim et al., 1991; Lavé

70   & Burbank, 2004; Lamb et al., 2011, 2013; Perkins et al., 2022), where they have also been linked to post-fire hazards (e.g., DiBiase & Lamb, 2019; Guilinger et al., 2020; Kean et al., 2011; Wells, 1987). Even in the absence of fire, however, it has been shown that bioturbation-driven dry ravel has the potential to contribute significantly to long term hillslope evolution and hazards in California (e.g., Black & Montgomery, 1991; Reed & Amundson, 2007), highlighting the need for clarity on the mechanics and physical controls on ravel processes.

75

The recognition of nonlocal transport characteristics of ravel and the failure of traditional continuum-based diffusive transport models to describe the heavy-tailed of travel distance distributions associated with nonlocal transport has led to the development of alternative models to more effectively describe nonlocal transport (e.g., Furbish and Roering 2013). Recent field experiments demonstrate that ravel particle travel distances are consistent with the Lomax distribution model theorized

80   by Furbish and Roering (2013) and refined by Furbish et al. (2021a). Using experimental clasts dropped at a range of burned and unburned field sites, Roth et al. (2020) showed that the parameters of a Lomax distribution capture a continuum of particle motion from local to nonlocal (i.e., light- to heavy-tailed distributions) as particle size increases or slopes get steeper or smoother. Furbish et al. (2021b) found that this model accurately described particle travel distances published in previous field experiments as well as new laboratory experiments. However, no study to date has conducted field experiments

85   representative of natural particle motion in a manner allowing model validation against observed post-fire deposits, nor have studies tracked the evolution of particle travel distances throughout post-fire recovery to explore the conditions under which dry ravel experiences nonlocal transport.

Here, we present a series of repeat particle drop experiments conducted in March 2021, July 2021, and March 2022 at a total

90   of seven positions on north- and south-facing hillslopes burned by the Santa Clara Unit (SCU) Lightning Complex fire in the Bay Area, CA in Summer 2020 (Fig. 1a-1b). Our selection of this site and particle drop experimental design were motived by observations of post-fire ravel entrainment by burrowing California ground squirrels and Botta's pocket gophers, which we attempted to simulate. We fit experimental particle travel distances to a Lomax distribution model to assess spatial and temporal variation in particle motion as vegetation recovered over the year and a half following the fire. Our experiments are

95   differentiated from prior studies by the use of experimental particles collected in situ at the field site (Fig. 1c) and corroboration of results with particle size distributions measured along the study hillslope. We use our experimental results along with field-measurement-based evidence of downslope coarsening of surface deposits to constrain the influence of

particle size, hillslope gradient, and aspect-dependent vegetation loss and recovery on post-fire sediment transport by dry ravel.

2 Methods

2.1 Field Methods

Field visits occurred from September 2020 to March 2022 (Fig. 1d), and experiments were conducted in March 2021, July 2021, and March 2022 (Fig. 1d, Images 2-4). In the following sections these three experimental epochs are described as Spring 2021, Summer 2021, and Spring 2022.

2.1.1 Study Site

Our field experiments were conducted in Santa Clara County, California, USA at the Arbor Creek Catchment in the Blue Oak Ranch Reserve (BORR), an experimental ecological reserve managed by the University of California Natural Reserve System since 1990 (Fig. 1a). The experimental catchment is located in the Diablo Range of the California Coast Ranges and is underlain by the Yolla Bolly Terrain of the Franciscan Assemblage (Dibblee & Minch, 2006). Sandstone, meta-graywacke, and shale outcrops were observed at the field area (Donaldson et al., 2023). The Arbor Creek Catchment has a drainage area of ~0.04 km^2 and elevation range of ~715-805 m a.s.l. The climate is Mediterranean, with warm, dry summers (August average 25°C) and cool, dry winters (January average 8°C). The majority of precipitation falls from October to May as rain (mean annual precipitation 600 mm), and streams are non-perennial (Donaldson et al., 2023).

The Arbor Creek Catchment consists of a generally south-facing slope (SFS) and a north-facing slope (NFS) draining to the west (Fig. 1a). The portion of the SFS used in our experiments is convex to planar with an average slope of 27 degrees and slopes up to 43 degrees adjacent to the channel. The portion of the NFS used in our experiments is planar to concave with an average slope of 31 degrees and slopes up to 35 degrees. Mobile material on the SFS generally consists of coarse, subangular to subrounded soil aggregates that move as coherent particles (Fig. 1b). On the NFS, the dominant species of mobile material is angular rocky colluvium, and a more limited fraction of soil aggregates is present relative to the SFS (Fig. 1b). Although soil compressive strength was not measured directly during our field visits, we observed that the soil at the SFS easily supported our weight with limited deformation. Where soil was present at the NFS, it would compact underfoot such that we left deep footprints, suggesting lower soil strength at the NFS relative to the SFS. Shallow soil moisture is generally greater at the NFS relative to the SFS (Donaldson et al., 2024), while soil depth is similar (30-80 cm) as is the mean depth to the saprolite-bedrock transition (5.7 m at the SFS, and 6.6 m at the NFS) (Donaldson et al., 2023).

The depth of soil at this site is assumed to bound the activity of burrowing rodents on the slope. These include both California ground squirrels (Otospermophilus beecheyi) and Botta's pocket gopher (Thomomys bottae). Observations of

freshly excavated granular material overlaying the burned surface in Summer 2020 (Fig. 1d, Image 1) suggest burrowing by rodents produces many of the loose particles observed on the hillslopes at the experimental site.
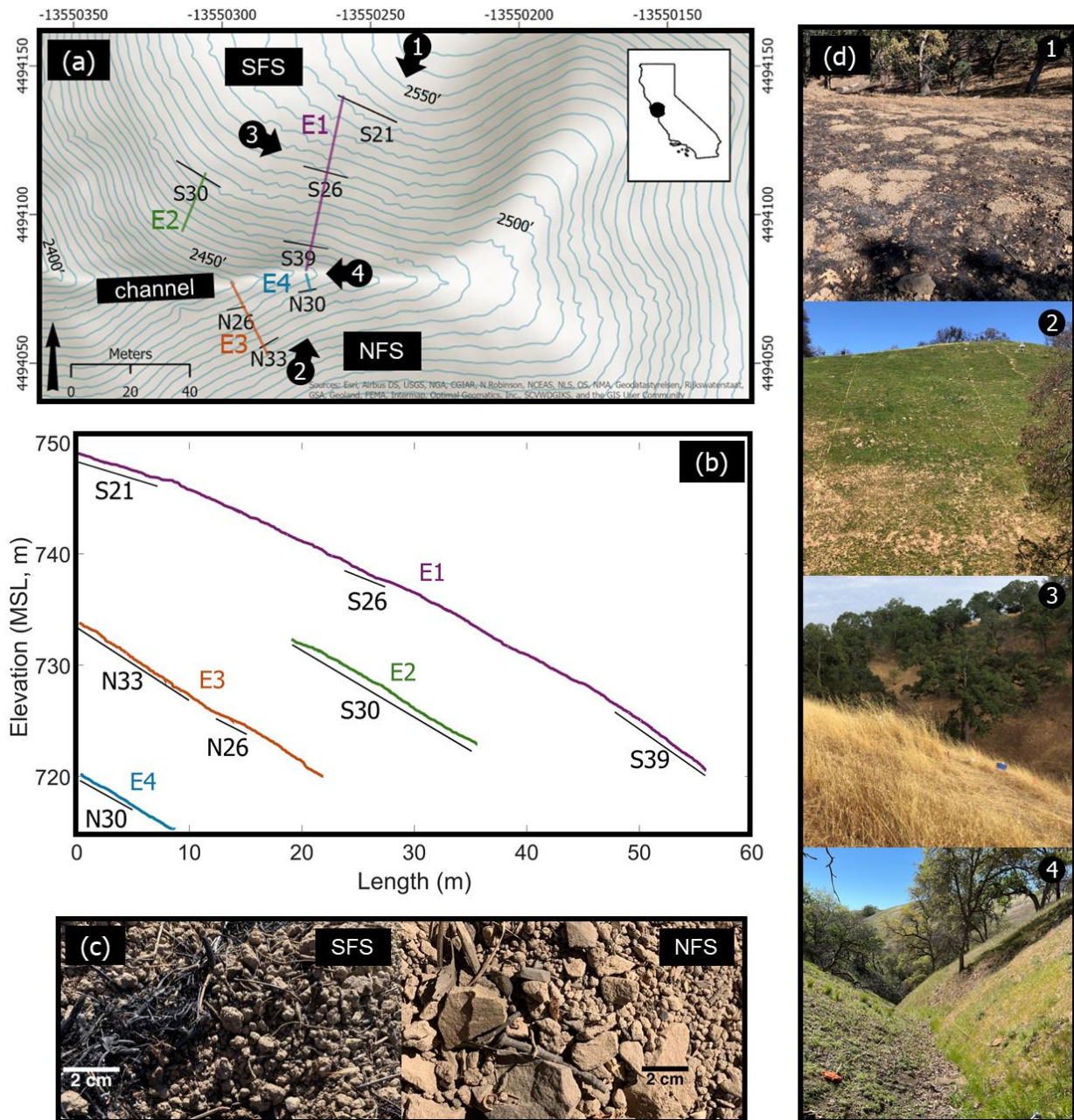
Figure 1: (a) The inset map indicates the location of BORR within California. The primary map presents the layout of the particle drop starting lines (black lines) for the 7 experimental sites in the Arbor Creek Catchment at BORR. Site labels reference aspect and average site slope angle (e.g., S21 corresponds to a south-facing site with slope of 21 degrees). Lines labelled E1-E4 indicate

cross sections corresponding to the elevation profiles shown in (b). The numbers 1-4 indicate the location at which site photos (d) were collected, with arrows representing photograph orientation. Coordinates are displayed as UTM Northing and Easting (m), NAD 1983. Elevation contours represent ~1.5 m (5 ft) intervals.

140 **(b) Elevation profiles interpolated from last returns of terrestrial laser scanner data at experimental sites. Black lines indicate the maximum distance any experimental particle travelled at each site.**

(c) Post-fire condition of surficial material at the SFS (soil, subrounded) and NFS (rock, subangular).

(d) Images (1-4) present various vantage points of the experimental catchment at different times including: one month post-fire (1), in Spring 2021 (2), in Summer 2021 (3), and in Spring 2022 (4). These photos exemplify the incineration (1) and initial recovery (2)
145 **of vegetation post-fire, followed by seasonal death (3) and regrowth (4).**

2.1.2 Pebble Counts and Particle Collection

We conducted pebble line counts to obtain grain size distributions of in situ particles at different slope positions on the SFS. During each count, we measured the intermediate axis of particles (rocks or soil aggregates) at every 10-cm mark on a
150 measuring tape laid along a 10 m contour-parallel transect. This approach is a common method of systematically sampling bed-surface material in rivers (e.g., Bunte & Abt, 2001; Hey and Thorne, 1983; Wohl et al., 1996). The 10 m transect length was set by the maximum along-contour distance over which the study hillslope remained relatively planar. The 10 cm sampling interval was chosen to be larger than the intermediate diameter of the largest particles observed at the study site, while still allowing ~100 measurements along each transect.
155

The Spring 2021 pebble counts were conducted at three transects initially identified as capturing the variable slope of the SFS (S21, S26, S39), which were also used for rock drop experiments, described below. Particle measurements in Spring 2021 were conducted with a ruler, with 1 mm precision at S21 and S26 and 5 mm precision at S39.

160 The extent of subsequent pebble counts in Summer 2021 and Spring 2022 was expanded to include 4 additional cross-slope transects, for a total of 7 transects spaced every 10 m downslope between the upper portion of the slope and the channel on the SFS. Particle measurements in Summer 2021 and Spring 2022 were conducted with a digital caliper, increasing measurement precision to 0.01 mm.

165 All in-channel particle measurements from Summer 2021 were collected above a leaf layer that accumulated in the months after fire, providing a lower bound to the timing of ravel deposition. The channel was then excavated down to the ash layer, such that all particle measurements from Spring 2022 represent material deposited between Summer 2021 and Spring 2022.

2.1.3 Particle Drops

Particle drop experiments were conducted at a total of 7 sites (Fig. 1a) to simulate ravel movement initiated by burrowing of California ground squirrels and Botta's pocket gophers. The experiments in Spring 2021 were conducted in conjunction with the pebble counts along only the three original SFS transects (S21, S26, S39). Initial experiments at these sites used only the particles from the pebble counts, which were dropped immediately after measurement. To ensure adequate characterization of particle travel statistics across the full grain size distribution, additional ad hoc experiments were conducted at sites S26 and S39 with particles collected on-site and sorted into bins with 0.5-cm resolution.

The preliminary results of the Spring 2021 pebble counts were used to identify three particle size classes for future experiments to span the measured range of particle sizes. In Summer 2021 we collected and spray painted several hundred particles from the experimental hillslope (rocks or soil aggregates, i.e., granules) falling within three intermediate axis dimension ranges of 0.25-1 cm (small), 1-2 cm (medium), and 2-3.5 cm (large) for use in particle drop experiments (Fig. 2). These particles were used in all experiments conducted in Summer 2021 and Spring 2022. The grain size distribution of each particle group was later characterized by hand measurement in the lab with a digital caliper. Measured intermediate axis dimensions for each size class fell within the ranges of 0.33-0.95 cm (small), 0.97-1.72 cm (medium), and 2.27-3.25 cm (large), with median (D50) values of 0.6, 1.3, and 2.8 cm, respectively for small, medium, and large particles (Appendix A, Table A2). We note that these values represent lower limits due to the possibility that some particles may have degraded in size without exceeding the particle size class limits. Based on the measured statistics of the particles used in Summer 2021-Spring 2022, we retroactively binned our data from Spring 2021 into small (0.25-0.75 cm), medium (0.75-2.25 cm), and large (2.25-3.25 cm) groups to make them as comparable as possible to later epochs given the 0.5-cm precision of Spring 2021 measurements.

Under these binning criteria, a range of 41 to 230 particle travel distances were included for each experimental particle size class at S21, S26, and S39 in Spring 2021. At site S21, randomly selected particles of intermediate diameter larger than ~2.25 cm were not present in sufficient quantities to include a large particle class in our analysis. Table A2 in Appendix A contains additional information on experimental particles for all epochs.

195 **Figure 2: Examples of small (left, blue), medium (middle, red), and large (right, pink) experimental particles used in particle drop experiments in Summer 2021 and Spring 2022. Ruler units are in cm.**

In addition to the three sites selected in Spring 2021, four additional drop locations were selected in Summer of 2021 to capture a broader range of surface conditions. This includes a site at the western nose of the SFS (S30) and three sites on the

200 NFS (N26, N30, and N33) as shown in Fig. 1a. The seven selected sites captured variation in aspect and slope over the study area. Particle drop experiments were conducted at all seven sites using the painted particles in Summer of 2021 and Spring of 2022 with a range of 100 to 200 particles dropped for each particle size class per site.

During the Summer 2021 experiments, grasses at the SFS experimental transects were observed to have heights of up to 1.3

205 m. At our experimental sites S21 and S26 these grasses were trimmed to ensure that particle distances could be feasibly measured and particles recovered after each experiment. Grasses were trimmed to ~15 cm, well above the estimated maximum particle bounce height at these sites, to avoid modifying the vegetative roughness encountered by the particles during transport.

210 During particle drop experiments (Fig. 3), particles were released from the middle of the palm with fingertips placed along the downhill edge of the starting line (Fig. 3a). This approach aimed to produce relatively consistent initial energies and rotational motion (Fig. 3b-3c) (as noted by Furbish et al., 2021b) reasonable for particles mobilized by the scratch digging typical of rodents at this site (Fitch, 1948; Kley and Kearney, 2006). To define a starting line, a tape measure was placed along contour (i.e., at a constant elevation) with a clinometer, and particles were released at regular 10-cm intervals (Fig.

215 3d). Particle travel distances were measured in the slope-parallel direction using rulers, meter sticks, or tape measures (Fig.

3d). Less than 5% of soil aggregate particles degraded during transport (as evidenced by loss of paint) such that they fell outside of the selected particle size ranges and were removed from the experiment.
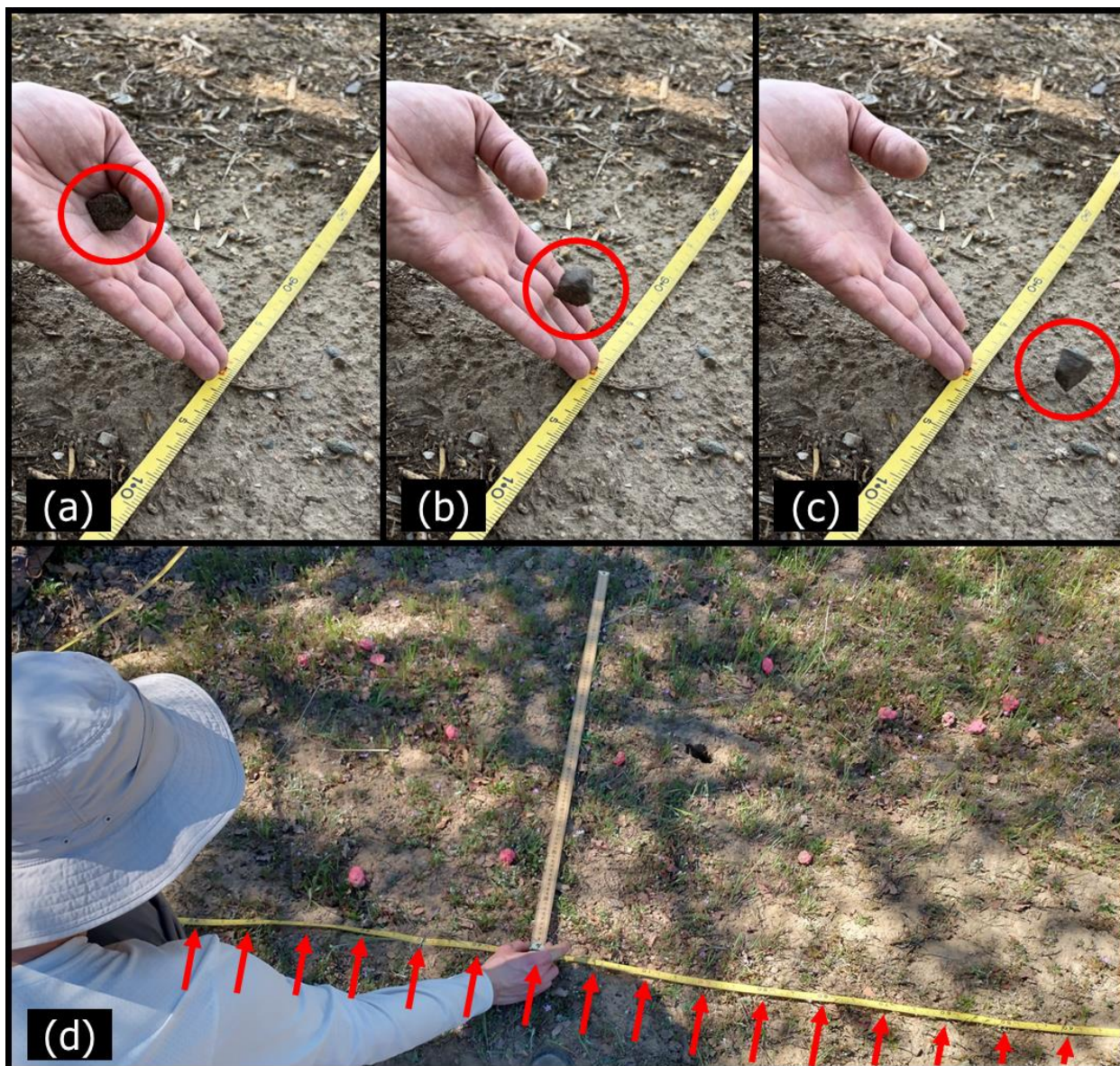
Figure 3: Experimental particle drop procedure, with panels a-c showing particle drop approach and panel d showing slope-parallel measurement of particle transport distance for large particle class (pink particles) at site N26 in Spring 2022. In a-c, red circles highlight position of particle during and after release. In d, red arrows represent particle drop positions at 10 cm intervals. Note photos in a-c were not collected at BORR.

2.1.4 Topographic Data

225 Topographic data used in our analyses was collected by UNAVCO with a Riegl VZ-2000 terrestrial laser scanner (TLS) between July 18 and July 20, 2021. Registration and georeferencing of point clouds was performed by UNAVCO. Point cloud resolution was generally between 0.1-2 cm.

We used TLS-derived point cloud data to define the surface slope at each particle experiment site. The software
230 CloudCompare was used to fit a plane to the unmodified point cloud of each particle drop experimental region with the built in "Fit Plane" tool. Due to the low density of points corresponding to vegetation relative to points collected at the mineral surface in the experimental regions, the vegetation did not qualitatively appear to impact our slope estimation approach. All slope measurements were also corroborated with field measurements collected with a clinometer. The experimental regions were visually identified with survey flags placed in the field prior to TLS collection. The size of these selected regions was
235 dependent on the width of the experimental drop zone and the maximum particle travel distance observed during the particle drop experiments described above.

2.2 Model Description

We used a Lomax model to represent particle travel distance exceedance probability R(x), also known as the survival function of particle travel distances or a complementary cumulative distribution. The exceedance probability can be related
240 to an associated spatial disentrainment rate P(x), or hazard function representing the conditional probability of a particle in motion being disentrained at a distance x downslope from its point of entrainment (Fig. 4). A Lomax distribution is capable of capturing both local and nonlocal transport regimes (Furbish et al., 2021; Roth et al., 2020), and generally acts as a constant function at low values of the travel distance, with a transition to a power law at greater values. This transition generally occurs at a value of B/|A| (Fig. 4a, 4c) (Milojević, 2010).

245

The modeled forms of R(x) and P(x) are defined in terms of the Lomax shape (A, dimensionless) and scale (B, dimensions of length) parameters (Roth et al., 2020):

$$R(x) = \begin{cases} \left(\dfrac{Ax}{B} + 1\right)^{-\frac{1}{A}} & \text{for } A \neq 0 \\ \exp\left(-\dfrac{x}{B}\right) & \text{for } A = 0 \end{cases} \tag{1}$$

250
$$P(x) = \frac{1}{Ax + B} \tag{2}$$

The Lomax distribution can represent a range of forms of R(x) and P(x) as the transport regime transitions from local (A≤0) to nonlocal (A>0) (Fig. 4). The form of the R(x) and P(x) described by the shape parameter A informs our physical understanding of the sediment transport regime. Although the Lomax distribution is fit to the survival function R(x) due to more limited potential for propagation of error from the cumulative probability distribution, the disentrainment function P(x) represents the physical process controlling travel distances and therefore informs our understanding of the mechanics of particle motion. Although our results are presented exclusively in terms of R(x) because these distributions were used to identify Lomax parameters A and B, we provide some background description of P(x) because of the physical relevance of the form of the distribution. R(x) explicitly results from P(x) and can be represented as such (Furbish and Roering, 2013).

$$R(x) = e^{-\int_0^x P(x')dx'} \tag{3}$$

The condition A<0 describing a light-tailed R(x) indicates that the likelihood of disentrainment P(x) will increase with distance asymptotically as particles approach position x=B/|A| (Fig. 4a). Particles are probabilistically unlikely to travel beyond this theoretical bounding distance, which we expect to increase with greater gravitational energy (for example, as particle size increases), an increased rate of conversion of gravitational energy to kinetic energy controlled by the surface gradient, and/or lower frictional losses from surface roughness. In this case, the model describes a transport regime of bounded motion, which is associated with "local" transport (Furbish et al., 2021b).

For A=0, R(x) is an exponential distribution and P(x) is equal to the constant 1/B, indicating the probability of disentrainment is equal at all travel distances and the transport regime can be described as uniform disentrainment (Fig. 4b). Regardless of the value of A, at short travel distances as x →0, P →1/B.

For A>0, the exceedance probability R(x) is heavy-tailed and the disentrainment rate P(x) decreases with distance along a slant asymptote P(x)=1/Ax after x=B/|A| (Fig. 4c). In this case, the spatially decreasing disentrainment probability represents the onset of runaway motion. The distance to this onset x=B/|A| is expected to decrease with greater gravitational energy (larger particle sizes) or conversion of gravitational to kinetic energy (steeper slopes) and lower frictional losses, each of which will lead particles to experience runaway motion at shorter distances. This condition represents the "nonlocal" transport regime (Furbish et al., 2021b).
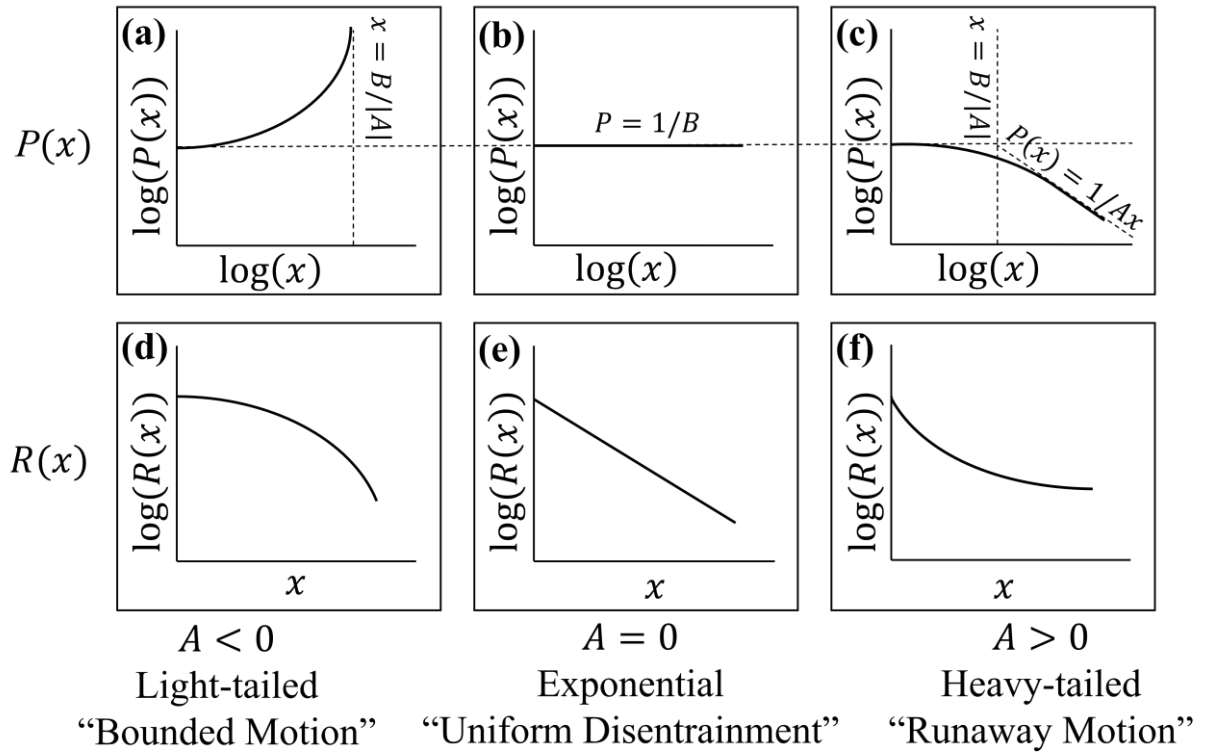
Figure 4: General form of the disentrainment rate P(x) (panels a, b ,c) and travel distance exceedance probability R(x) (panels d, e, f) corresponding to different values of the Lomax shape parameter (A) where x represents downslope travel distance, modified after Roth et al. (2020).

2.3 Initial Processing of Empirical Data

Preliminary processing of empirical travel distance data was conducted to prepare data for Lomax distribution fitting. Particle motion was non-stochastic immediately after release from the palm due to our use of a consistent approach for initiating particle motion (Fig. 3a-3b). Stochastic motion occurred after contact with the mineral surface, which induced random components of motion as particles bounced and tumbled. In our experimental approach, the disentrainment rate may be anomalously low relative to naturally occurring transport prior to the onset of stochastic motion, especially for the smallest particles (Furbish 2021b). To ensure that only stochastic particle motion associated with particle-surface interactions (as opposed to motion dominated by initial conditions associated with experimental procedures) was captured and avoid the potential influence of unrealistically uniform initial particle velocities, we left-truncated all empirical travel distance exceedance distributions at a distance of 1 cm (i.e., removing travel distances ≤ 1cm). We note that the onset of stochastic motion may vary for particles of different geometry, as more rounded or angular particles may initially experience tumbling or a random oblique motion, respectively. We selected a single left truncation distance for combined distributions

of different particle geometries rather than separating particles by geometry or composition (soil or rock) in order to achieve our goal of identifying a general trend for a given range of particle sizes. We selected the truncation value of 1 cm through a combination of visual analysis of the raw empirical R(x) data and consideration of the median intermediate diameter of the smallest particles involved in our study (~0.64 cm), which is approximately half the truncation distance (e.g., Furbish et al., 2021b).

After truncating travel distance measurements ≤ 1 cm, we calculated an empirical cumulative distribution, F(x) for each experimental travel distance dataset. We normalized F(x) by a factor of N+1 (where N is the number of samples) under the assumption that the cumulative probability of empirical data remains below 1 due to the finite number of samples (e.g., Furbish 2021b). Three of the seven sites were then assigned a Type-I (right) censor distance (Appendix A, Table A3) based on the distance to physical barriers that terminated particle travel such as the channel at the base of the slope (S39, all epochs), dense piles of vegetative debris (S30, Summer 2021), or trails caused by human activity on the slope (N33, Spring 2022). In cases where censorship was necessary, particle travel distances exceeding the censor distance were excluded from the empirical distribution. If a physical barrier was not present at the time of our experiments, then no Type-I censorship was applied. We then calculated the empirical exceedance distribution R(x) as the complementary cumulative distribution, or R(x) = 1-F(x).

2.4 Optimization of Lomax parameters

Lomax parameters describing the transport regime of our experimental ravel simulations were optimized by fitting a Pareto Type II (Lomax) distribution (Equation 1) to the empirical travel distance exceedance probability R(x). We optimized Lomax parameters A and B through an ordinary least-squares regression. Our optimization approach is identical to that of Roth et al., (2020) with the Nelder-Mead Simplex selected for minimization, implemented as described in Lagarias et al. (1998). This algorithm is highly efficient, simple to implement, and capable of optimizing a wide range of objective functions. Because this method was not guaranteed to converge at a local minimum without an initial parameter estimation of reasonable quality, a trust region regression capable of handling poor initial guesses was first implemented to obtain initial estimates of A and B (Sorensen & Moré, 1983).

Error estimations presented in our results were calculated using a bootstrap procedure in which each R(x) was resampled with replacement 10000 times with one of the parameters A or B individually fixed while the other was calculated (per Roth et al., 2020). The standard deviations of the estimated parameters, σ_A and σ_B, respectively were used to denote their uncertainty as the standard error, and the uncertainty in B/|A|, denoted $\sigma_{B/|A|}$ was calculated through the method of moments using these standard deviations and the covariance of the bootstrapped parameters, σ_{AB}, as described in Equation 4.

$$\sigma_{\frac{B}{|A|}} = \sqrt{\left(\frac{B}{A^2}\sigma_A\right)^2 + \left(\frac{1}{A}\sigma_B\right)^2 - \frac{2B}{A^3}\sigma_{AB}} \tag{4}$$

For cases in which nonlocal transport was identified with A>0, the tail is the sparsest region of the empirical data and may be underrepresented. This issue is exacerbated by a low sample number N. As noted by Furbish (2021b), parametric values estimated with N<1000 should be accepted with skepticism, especially for heavy-tailed distributions, for which variability in R(x) increases. Any censored distributions may only have a small portion of the exceedance probability represented in the experimental data, exacerbating underrepresentation of the tail. Unfortunately, N>1000 was deemed to be impractical in our field experiments due to the extensive time required to drop, measure, and collect the in situ particles at a large number of sites as described in Sect. 2.1. This is a perspective shared by other similar field studies such as DiBiase et al. (2017), who dropped between 43 and 93 particles for their various size classes and Roth et al. (2020), who dropped ~100 particles of each size class per site. Given the logistical limitations of our experiments, we therefore acknowledge uncertainty in A, particularly in our ability to distinguish heavy-tailed and light-tailed distributions for values of A close to 0.

2.5 Estimating Mean Travel Distance and Frictional Coefficient

Besides allowing evaluation of the transport regime (A) and length scale of transport (B), the Lomax parameters A and B allow calculation of mean travel distance (μ_x) and a frictional coefficient describing energy lost due to particle collisions with the mineral surface and vegetation (μ) as described in Furbish et al. (2021b). Note that μ is not a Coulomb-like friction coefficient, but describes the efficacy of frictional losses due to particle-surface collisions that extract translational energy. For additional discussion, see Furbish et al. (2021a, 2021b).

The mean value μ_x of a Lomax distribution is defined as

$$\mu_x = \frac{B}{1-A} \quad A < 1. \tag{5}$$

Note that μ_x only exists when A<1 (Furbish et al. 2021b); for heavy-tailed distributions with A≥1, the mean is undefined.

To estimate μ, we follow the approach of Furbish et al. (2021b),

$$\mu = S - \frac{E_0\left(A - 1 + \frac{1}{\gamma}\right)}{Bmg\cos\theta} \tag{6}$$

where S is hillslope gradient, θ is slope angle in radians, m is particle mass, and g is acceleration due to gravity (9.81 m/s^2). E_0 is the initial kinetic energy, and γ, the ratio of the arithmetic and harmonic means of particle energy, was set to 1.5 following Furbish et al. (2021b).

In our use of equation 6, we estimated particle potential energy as a replacement of initial particle kinetic energy with an assumption that all potential energy available to each particle due to the elevated position of release (Fig. 3a) was converted to kinetic energy by the time the particle contacted the ground surface. Potential energy was calculated as mgh, with a constant release height above the ground, h, of 10 cm for all particle sizes. We estimated m by assuming a spherical particle form and calculating particle volume from the median intermediate particle axis. We then assumed a particle density of 1200 kg/m^3 to obtain m.

3 Results

Presented results describe observations and experimental results following our field visits at the Arbor Creek Catchment. These include a qualitative assessment of vegetation condition through time, grain size distributions from our pebble counts, and Lomax parameter values (A and B) derived from our particle drop experiments.

3.1 Qualitative Vegetation Assessments

To provide context for the results of our particle drop experiments, we present qualitative descriptions of vegetation at the SFS and NFS and how vegetation structures evolved as the site recovered post-fire. The SFS is dominated by annual grass species (e.g., Avena sp., Bromus diandrus). The NFS is dominated by blue (Quercus douglasii), black (Q. kelloggii), and valley (Q. lobata) oaks, with sparse annual grasses and prevalent lichens and moss. The grassy vegetation on these slopes undergoes seasonal cycles, with growth through the spring and senescence in late summer as rainfall ceases and temperatures increase. This is particularly noticeable at the SFS, which receives more insolation and has a larger population of grasses relative to the NFS. Donaldson et al. (2024) focused on aspect-dependent evapotranspiration rates at our field site and found that the SFS, in contrast to most south-facing aspects in the Southern hemisphere that receive more insolation than their north-facing counterparts, had lower rates of evapotranspiration than the NFS due to oak tree water uptake from weathered bedrock at the NFS. While the NFS had greater rates of evapotranspiration than the SFS, our observations of soil texture and the findings of Donaldson et al. (2024) indicate the NFS generally had higher levels of shallow soil moisture. Donaldson et al. (2024) proposed that the different hillslope-scale vegetation structures at the SFS and NFS are driven by factors including higher air temperature and reduced shallow soil moisture at the SFS, as the SFS is grass-dominated and the NFS is oak tree-dominated, though mosses and short grasses are present at the NFS.

In addition to observations of different vegetation structures and soil moisture, different fire behavior at the SFS and NFS resulted in observations of variable burn severity between aspects during our field visits. Following the August 2020 SCU Lightning Complex fire, grasses were singed down to a roughly uniform ~0-3 cm height, but generally still present at the soil surface on the SFS. We did not observe alteration of granular aggregate structure or damage to fine root structure. Based on

these characteristics and the observed recovery of vegetation within one year, the SFS was generally burned at low severity

385 (Parsons et al., 2010). The NFS experienced a wider range of soil burn severities ranging from unburned to high, although the majority of the slope demonstrated low burn severity. Lichens and moss were observed to be unaltered in some areas post-fire. Limited patches of high burn severity were present where downed trees or branches were incinerated. Within these patches, the organic woody and soil components were completely consumed, several cm of white ash was present, and soils demonstrated disaggregation and oxidation typical of the extreme temperatures associated with burning of downed logs (e.g.,

390 Mataix-Solera, et al. 2011). On both NFS and SFS, the intensity of burrowing activity after the burn was clearly visible due to the difference in color of the charred surface and lighter excavated soil (Fig. 1d, Image 1).

Along with aspect-dependence of burn severity, different post-fire vegetation structures were observed at the SFS and NFS. These structures are relevant when considering the evolution of particle transport over time. Here, we provide our qualitative

395 observations of vegetation and images of typical vegetation structures at each aspect. Within 7 months of the fire, vegetation (grass) had begun to regrow on the SFS. During the Spring 2021 experimental period, the vegetation was several cm high and covered the majority of the SFS, though it was fairly sparse (Fig. 1d, Image 2; Fig. 5a). Where vegetation was denser, it was observed to resist the downslope motion of particles mobilized by burrowing California ground squirrels (Fig. 5b). By July 2021 the SFS vegetation had experienced seasonal die-off, but residual dry matter ranged from roughly 30 cm to 1.3 m

400 in height (Fig. 1d, Image 3; Fig. 5c). In Spring 2022, live vegetation had regrown to a height of several cm to 1 m and leaf litter and dead grasses were present on the mineral surface (Fig. 5d). The leaf litter and dead grasses increased surface roughness relative to our first experimental period, as these materials had been recently incinerated prior to our experiments in Spring 2021. The mineral and vegetative surface roughness in Summer 2021 and Spring 2022 qualitatively appeared similar, though the height of the dead vegetation was greater in Summer 2021, and the live vegetation was observed to be

405 less brittle and more resistant to displacement when impacted by traveling particles in Spring 2022.

Figure 5: Vegetation conditions at south facing slope (SFS) through experimental epochs. (a) in Spring 2021 vegetation was generally short and sparse, though in some regions dense vegetation was observed as shown in (b), vegetation supporting a deposit of granular material generated from a California ground squirrel burrow. (c) By Summer 2021 vegetation had regrown and died. Panel c shows how this dead vegetation at site S21 acted as a barrier to our large particles. (d) In Spring 2022, there was a mixture of live and dead vegetation.

410

The NFS experienced more limited post-fire evolution of vegetation compared to the SFS. Throughout all experimental
415   periods, the surface characteristics of the NFS appeared relatively unchanged based on vegetation density and moss cover,
though most grasses were dead in Summer 2021 (Fig. 6a) and a mix of live and dead vegetation was present in Spring 2022
(Fig. 6b).

Figure 6: Typical vegetation conditions on the NFS during experimental epochs. (a) Site N26 in Summer 2021.
420   **Although grasses are present, their density is lower than at the SFS in the same experimental epoch and more of the**
mineral surface is visible. (b) Site N33 in Spring 2022. Mosses and grasses are present, and vegetation is less dense
than at the SFS. Note the presence of more angular, rocky particles at the surface in contrast to the soils on the SFS.

3.2 Pebble Counts

425   The particle size distributions measured by pebble counts during each study epoch are presented in Fig. 7. The median
diameters (D_{50}) of our three selected particle size classes for Summer 2021 and Spring 2022 are indicated on all plots.

In Spring 2021, particle size distributions appear similar along all three transects at which measurements were collected (0 m, 20 m, and 50 m transects roughly corresponding to the positions of sites S21, S26, and S39). We note that because measurements taken along the 50 m transect near the hillslope toe were recorded at 0.5 cm precision, this distribution is only coarsely comparable with other distributions. In Summer 2021, we observed notable downslope coarsening in surface particles in the lower transects near the hillslope toe where the slope increases. The material collected at "channel S", or the channel along the base of the SFS, approximately 10 m below the 50 m transect, was coarser than the material on the hillslope, with a median value over twice that of the lowest hillslope transect at 50 m (Appendix A, Table A1). By Spring 2022, downslope coarsening in the channel was still evident, but had declined substantially.
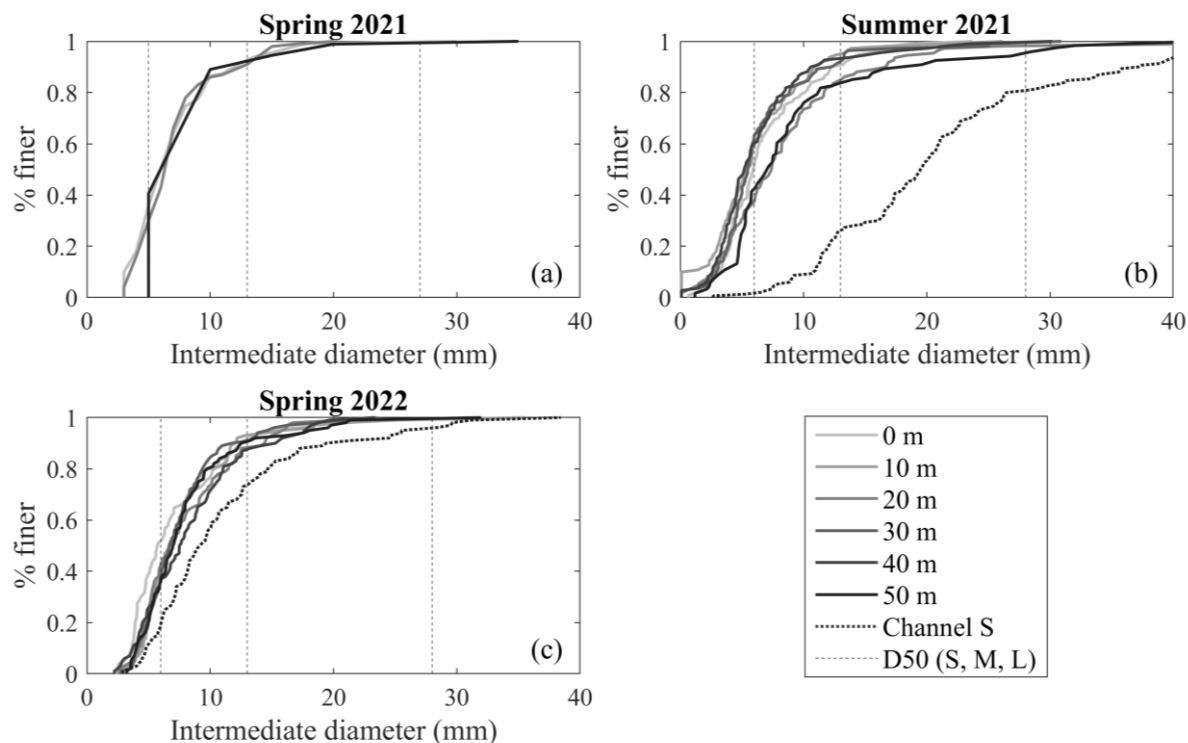
Figure 7: Particle size distributions from pebble counts conducted on cross-slope transects along the study hillslope during (a) Spring 2021, (b) Summer 2021 and (c) Spring 2022. . Distances 0 - 50 m represent each transect's downslope distance from experimental particle drop site S21. The extent of counts in Spring 2021 was limited to only 0, 20 and 50 m transects, and particle sizes at 50 m were collected at a reduced measurement precision (0.5 cm). Dashed lines represent the median diameters (D50) of the three particle size groups used in Summer 2021 and Spring 2022 experiments (S = 0.6 cm, M = 1.3 cm, and L = 2.8 cm). Note the 95th percentile of Channel S particles and above are excluded from the plot in panel b to aid comparison between epochs. The largest of these particles had an intermediate diameter of 88 mm, and the remainder 51 mm or less.

3.3 Evolution of Lomax Parameters with Site Recovery

Figures 8 and 9 show variation in model R(x) and associated empirical travel distance data through time for each experimental site and particle size combination. Note that the number of dropped particles in each experimental group (N) and estimates of A, B, σ_A, and σ_B may also be found in Appendix B, Table B1. See Appendix B, Fig. B1-B7 for individual empirical datasets, model fits, and visualizations of variability in the form of R(x) with estimated σ_A. Figure 8 illustrates the evolution of R(x) at all SFS sites, while Fig. 9 shows the evolution of R(x) at all NFS sites. Note that versions of Figs. 8 and 9 with equal scaling of the horizontal axes for each experimental site are available in Appendix B (Figs. B8 and B9). Experiments at sites on the NFS and the S30 site were only conducted in Summer 2021 and Spring 2022.
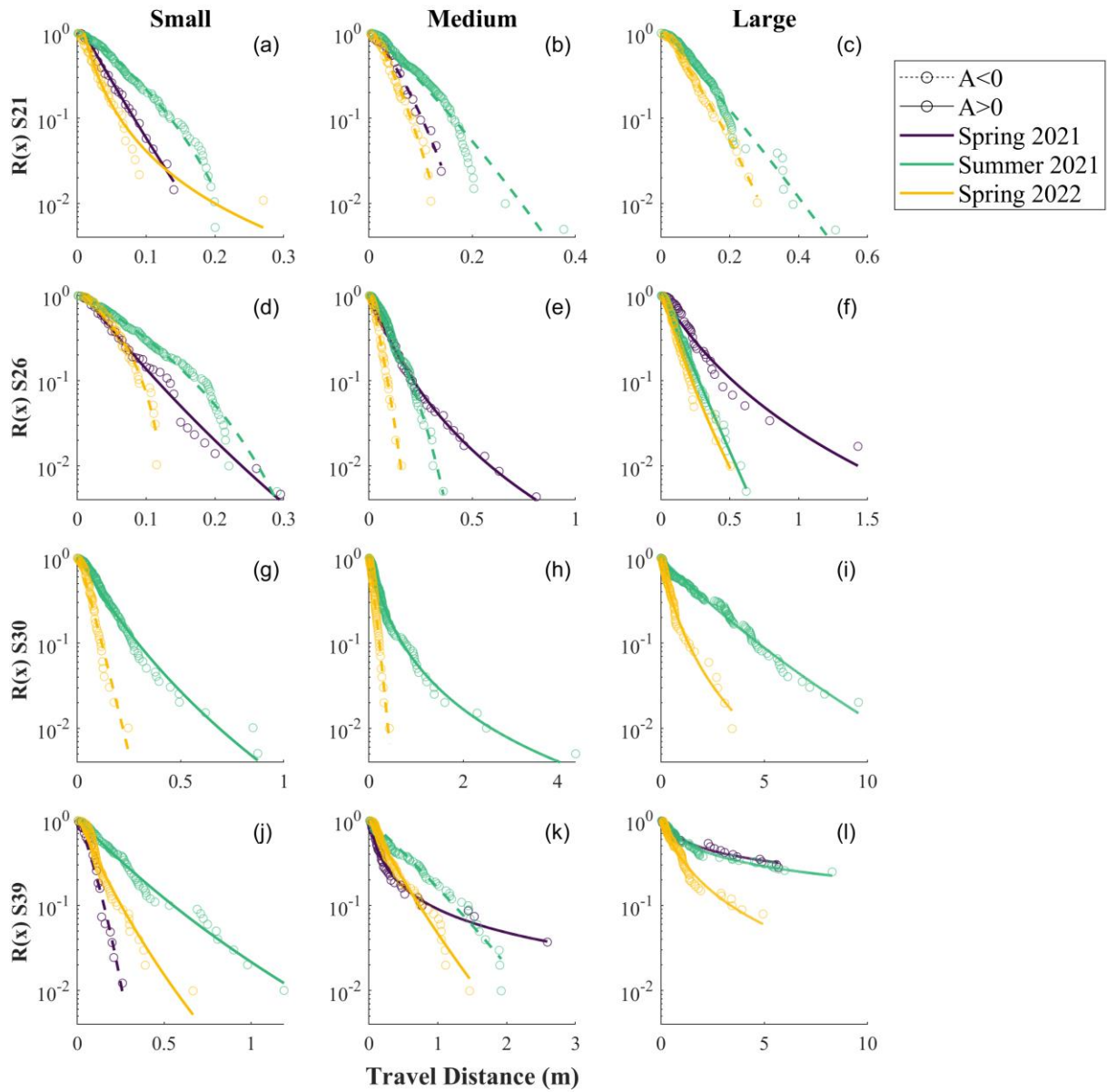
Figure 8: Empirical and modeled travel distance exceedance distributions R(x) for all SFS sites. Dashed lines indicate models with A<0 (bounded motion) and solid lines indicate models with A>0 (runaway motion). Open circles represent empirical data. Columns correspond to particle sizes (small, medium, large) while rows indicate experimental site.
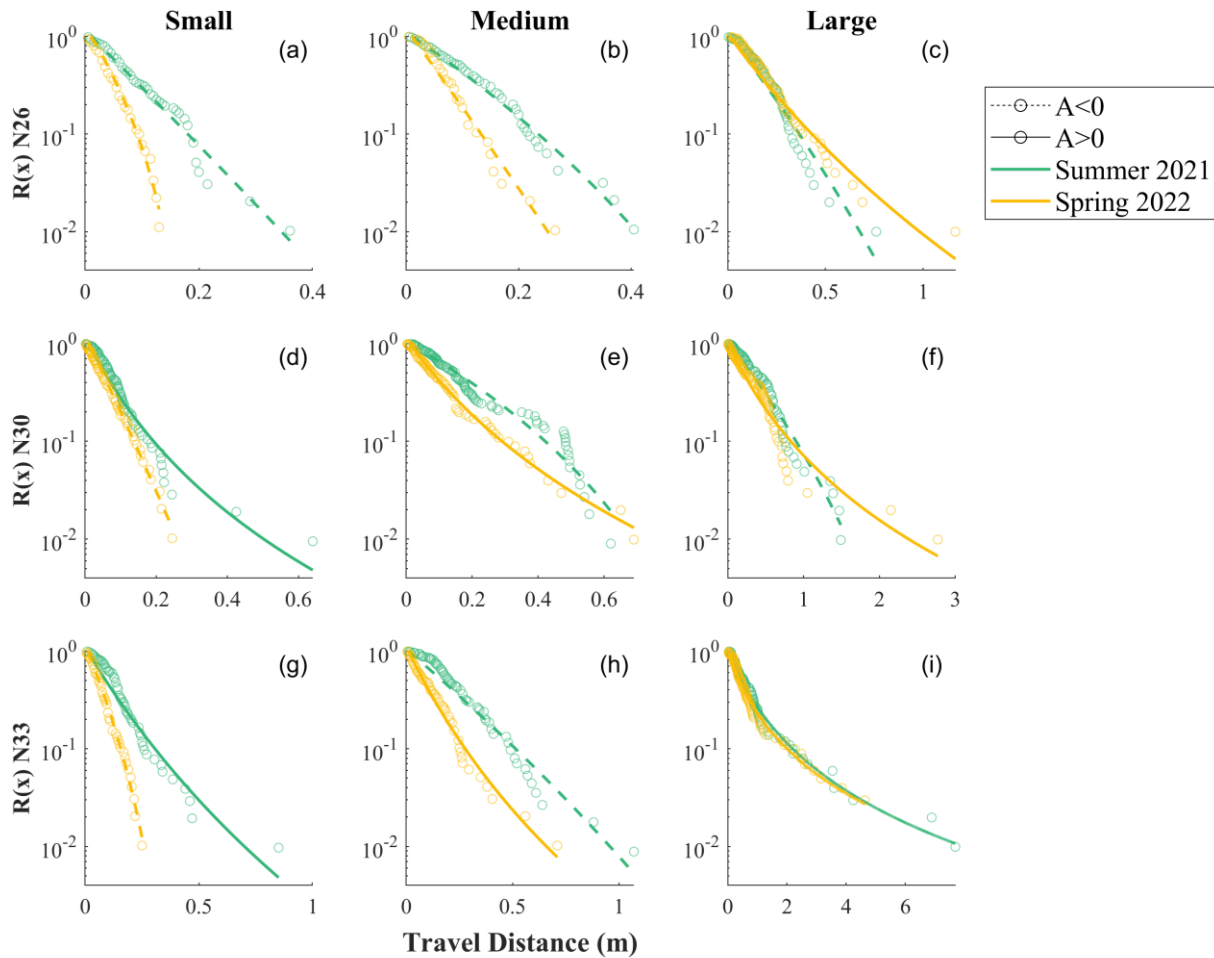
Figure 9: Empirical and modeled ravel distance exceedance distribution R(x) for all NFS sites. Dashed lines indicate models with A<0 (bounded motion) and solid lines indicate models with A>0 (runaway motion). Open circles represent empirical data. Columns correspond to particle sizes (small, medium, large) while rows indicate experimental site.

Figures 8 and 9 indicate that nonlocal transport of the in situ particles in our experimental catchment occurs across a range of particle sizes, hillslope gradients, and aspects as evidenced by the presence of heavy-tailed travel distance exceedance distributions (solid lines). In Fig. 8 and 9, heavy-tailed distributions are shown to be most prevalent for the largest particles, and their occurrence decreases for smaller particle sizes. More heavy-tailed distributions are also observed across the range of hillslope gradients and particle sizes in the first experimental periods during earlier stages of post-fire site recovery, with a general transition to light-tailed distributions as the site continued to recover. Alternative results using a 1.75 cm M versus L binning threshold rather than 2.25 cm for Spring 2021 are presented in Table A4, and broadly show similar results.

No single trend in A vs. time elapsed since the fire can be consistently identified across all sites and particle sizes. It is therefore more useful to consider the evolution of A across different combinations of particle size, hillslope gradient, aspect, and experimental epoch. Note that in our presentation of trends in Lomax parameters in Figs. 10-14 (A and B), we include

475   the standard error ($\pm\sigma_A$, $\pm\sigma_B$).

The evolution of A across all experimental parameter combinations is presented in Fig. 10. Mirroring results from Figs. 8 and 9, Fig. 10 shows positive A values (i.e., nonlocal transport) in our dry ravel simulations for all particle sizes and indicates that as particle size increased at both the NFS and SFS, the largest A value observed also increased. At the SFS, A

480   values diverged with time for small particles (Fig. 10d) while A values converged for medium and large particles (Figs. 10e-10f). The range of A between the NFS and SFS for medium (Figs. 10b and 10e) and large particles (Figs. 10c and 10f) also became more similar with time post-fire. Note that in Fig. 10, σ_A values are sufficiently large to induce uncertainty in the sign (and therefore transport regime) of A for 13 of our 51 combinations of particle size, hillslope gradient, aspect, and experimental epoch (see Appendix B, Table B1).
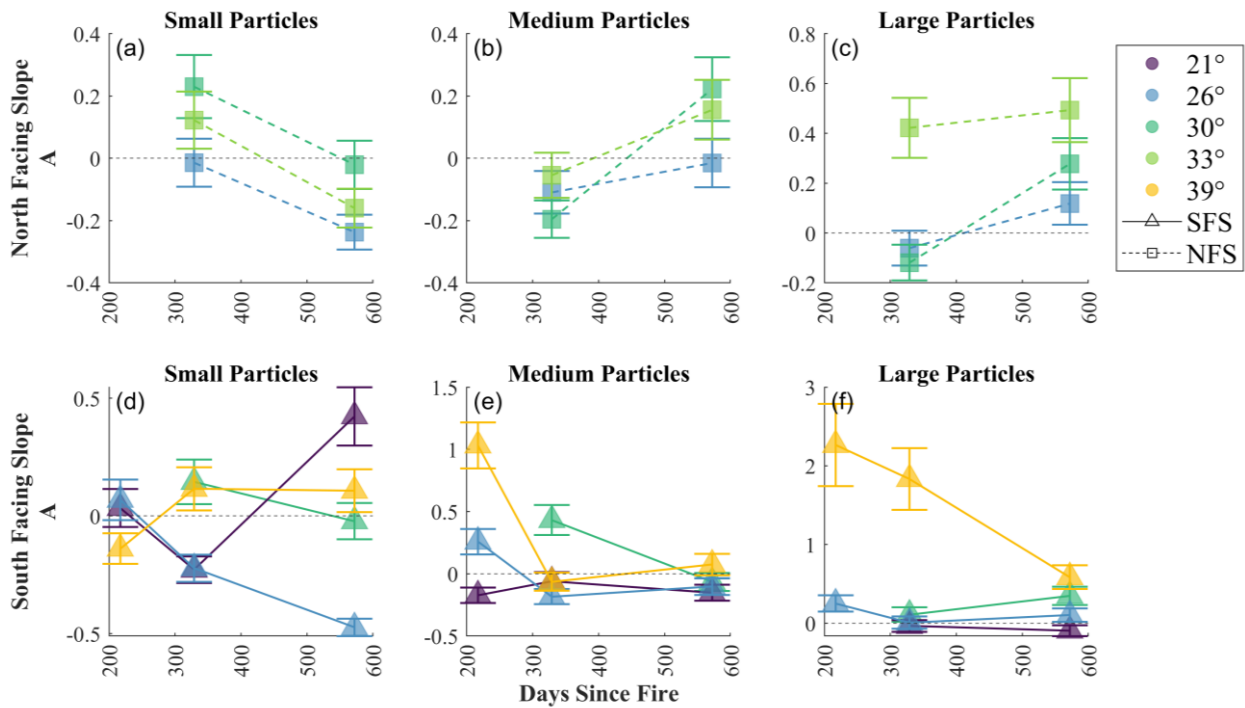
485

Figure 10: Values of Lomax shape parameter A for all combinations of particle size class, slope angle (°), and experimental epoch, on the a-c) north-facing (NFS) and d-f) south facing (SFS) study slopes. Error bars represent standard error ($\pm\sigma_A$) of A obtained from bootstrapping. Field visits occurred 217, 329, and 572 days post-fire. There is a dashed line at A = 0, the boundary between heavy-tailed (A>0) and light-tailed (A<0) Lomax distributions.

490 Figure 11 shows changes in A, B, and the reciprocal of mean travel distance ($1/\mu_x$) with hillslope gradient. This figure shows that A, B, and μ_x generally increased as slopes steepen for all observed particle sizes and experimental epochs, although exceptions occur among small and medium particles on lower slopes.

495 A values for the transport regime of the largest particles demonstrate larger increases with increasing hillslope gradient than those of small or medium particles in Spring 2021 and Summer 2021 (Fig. 11a-b). Figure 11 also suggests a transition from a more nonlinear relationship between A and gradient (Fig. 11b) to a more linear relationship (Fig. 11c) with time since fire for large particles.

500 Besides showing an increase in the length scale of transport with gradient, Fig. 11d-i also illustrate the consistent decrease in the length scale of transport between Summer 2021 and Spring 2022 (see Appendix C, Figs. C1-C2 for additional visualizations).
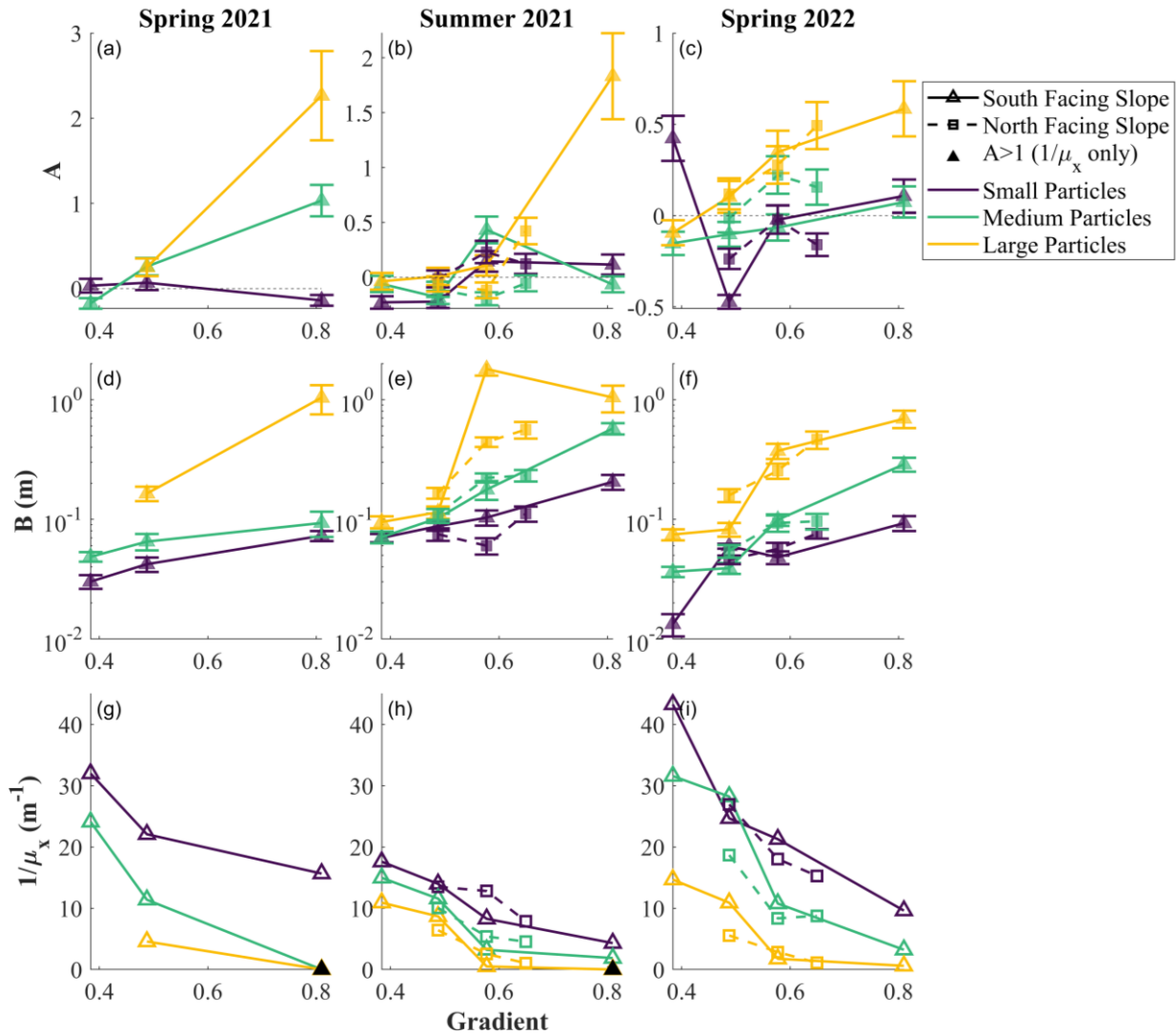
Figure 11: a-c) Trends in A with hillslope gradient during a) Spring 2021, b) Summer 2021, and c) Spring 2022; note differences in vertical axes between sub-plots. There is a dashed line at A = 0, the boundary between heavy-tailed (A>0) and light-tailed (A<0) Lomax distributions. d-f) Trends in B with hillslope gradient for each experimental particle size during d) Spring 2021, e) Summer 2021, and f) Spring 2022. g-i) Trends in the reciprocal of mean travel distance ($1/\mu_x$) with hillslope gradient for each experimental particle size during g) Spring 2021, h) Summer 2021, and i) Spring 2022. Undefined values of $1/\mu_x$ ($\mu_x = \infty$ for A ≥ 1) are represented by filled black markers and plotted at a value of 0 (medium and large particles at S39 in Spring 2021 and large particles at S39 in Summer 2021).

Figure 12 illustrates trends in A, B, and μ_x with particle size for each experimental site. Each of A, B, and μ_x generally increased with particle size. Figure 12g-i suggests an exponential-like relationship between μ_x and particle size.
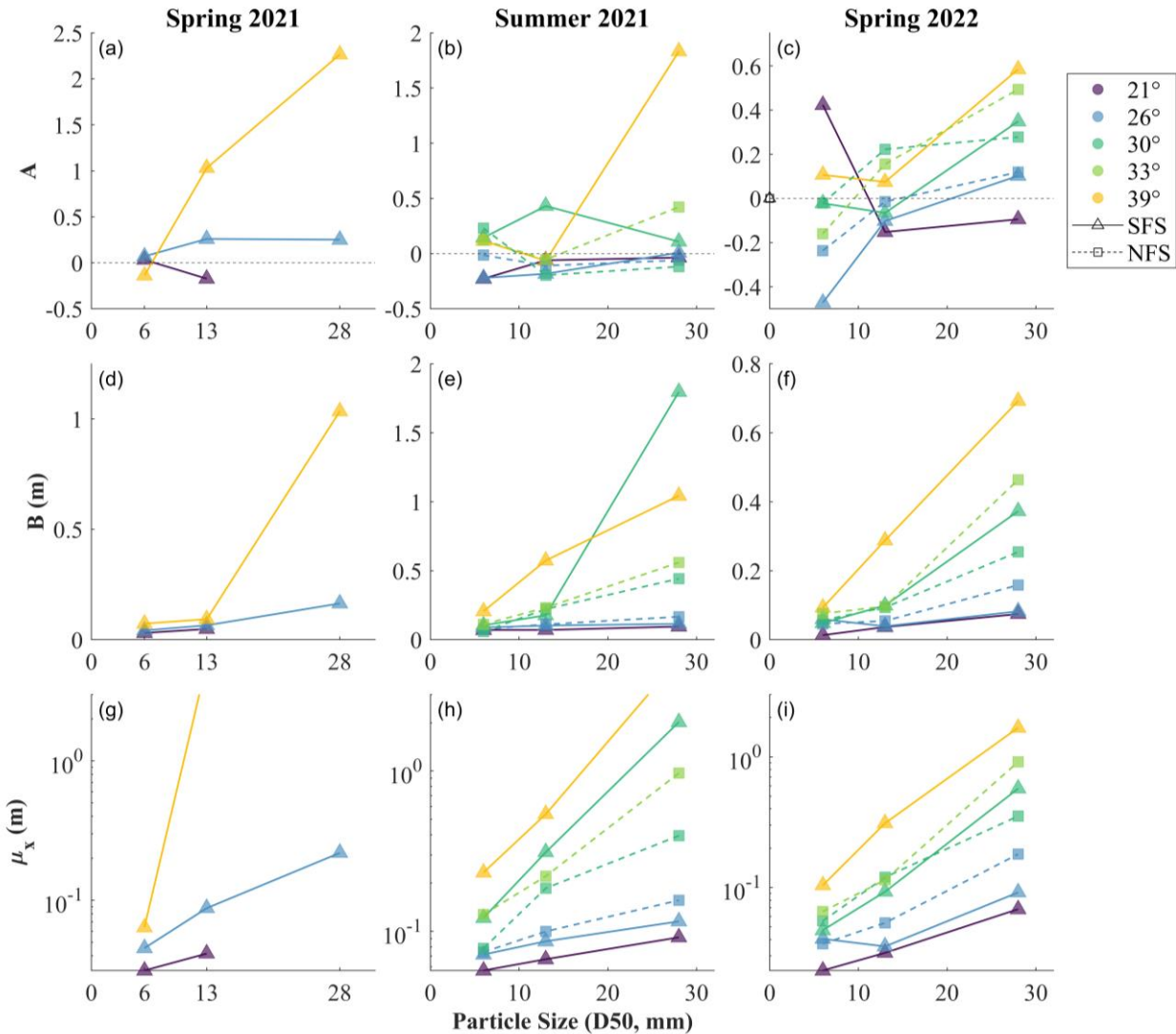
Figure 12: a-c) Trends in A with particle size; note differences in vertical axes between sub-plots. There is a dashed line at A = 0, the boundary between heavy-tailed (A>0) and light-tailed (A<0) Lomax distributions. **d-f)** Trends in B with particle size; note differences in vertical axes between sub-plots. **g-i)** Trends in mean travel distance (μ_x) with particle size. Values of $\mu_x = \infty$ (for A ≥ 1) are plotted at $\mu_x = 5$ (above vertical axis extent) to allow visualization of trends in μ_x. These values include medium and large particles at S39 in Spring 2021 and large particles at S39 in Summer 2021. SFS = south facing slope, NFS = north facing slope.

To evaluate differences in the frictional energy losses experienced by differently sized particles at our experimental sites, we calculated a friction coefficient μ as described in Sect. 2.5. Figure 13 shows that frictional losses generally increased through time for medium and large particles, although μ decreased in some cases between Summer 2021 and Spring 2022. There is no clear pattern in frictional losses of small particles through time where data is available for all epochs. Additional figures presenting the relationship between μ and gradient organized by epoch and site are available as Appendix C, Figs. C3-C4.
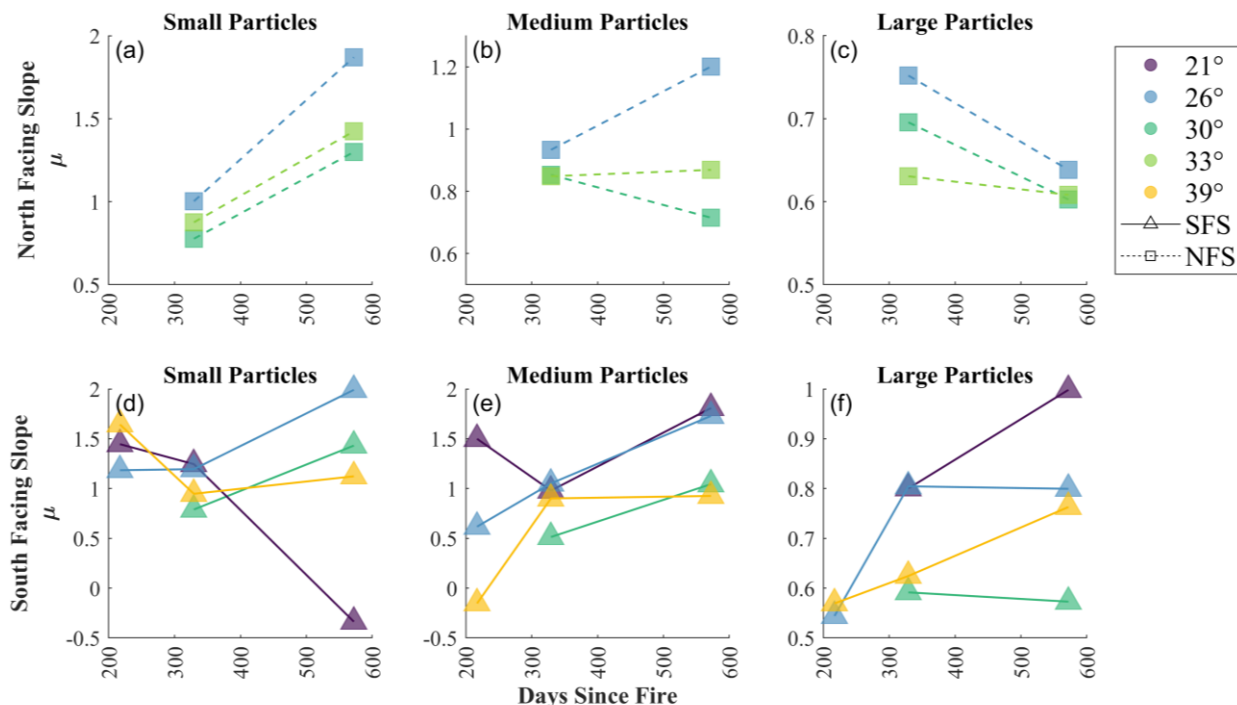
Figure 13: Values of coefficient of friction (μ) for all combinations of particle size class, slope angle (°), and experimental epoch, on a-c) the north-facing study slope (NFS) and d-f) the south-facing study slope (SFS). Field visits occurred 217, 329, and 572 days post-fire.

4 Discussion

Here, we consider the results of our pebble counts and dry ravel simulations to evaluate the influences of particle size, aspect, and slope on dry ravel as the time since the Arbor Creek Catchment burned increased. We also consider evidence of downslope coarsening of particle size at the SFS. Our experimental results are compared against previous field and lab experiments exploring dry ravel transport regimes, and we provide suggestions for additional data collection efforts relevant to those who apply the Lomax model to similar in situ particle transport experiments.

4.1 Transport Dependence on Site Conditions and Particle Size

The heavy-tailed travel distance exceedance distributions we observe provide clear evidence of nonlocal transport at a variety of particle size and slope combinations (Figs. 8-10 and 11a-c). Since these results represent the behavior of in situ particles under experimental conditions intended to simulate a primary particle entrainment process at this site (burrowing), these results suggest that nonlocal transport does occur within the natural range of particle sizes, slopes, and post-fire surface conditions at this site.

545 Overall, larger particles on steeper slopes were more likely to exhibit nonlocal transport over long distances. The heaviness of distribution tails (A), the length scale of transport (B), and mean travel distances (μ_x) in any experimental epoch generally increased with particle size and gradient on both study slopes (Figs. 11 and 12). Our estimated μ values suggest that frictional energy losses (evaluated with μ) were also greater for small and medium particles, and vegetation and mineral roughness were less effective in reducing particle energy as hillslope gradient increased (Fig. 13). These findings are

550 consistent with expected controls on particle disentrainment, as larger particles have a larger component of effective gravitational energy due to their higher mass and are therefore less affected by surface roughness (e.g., Furbish et al., 2021b; Gabet and Mendoza, 2012; Roth et al., 2020). We find less consistent behavior at low gradients, especially for smaller particle sizes, which often demonstrate higher A values than medium or even large particles (discussed below).

555 Figure 11g-i emphasizes that both particle size and vegetation structures control the slope at which a transition to runaway motion may occur. Theoretically, particles rolling down a rough surface would exhibit a linear decline in the reciprocal of the mean travel distance, or $1/\mu_x$ with increasing gradient before approaching 0 (at $\mu_x= \infty$), corresponding to a critical gradient at which particles are unlikely to be trapped by topography (Furbish et al., 2021b; Samson et al., 1999). For all particle groups, our data suggest that the critical gradient likely increased with time since fire due to vegetation regrowth as

560 evidenced by increases in $1/\mu_x$ at most sites with time (with the exceptions of medium particles on the lowest slope and all small particles between Spring and Summer, 2021). However, our data also suggest that the critical gradient is particle size-dependent. The value of $1/\mu_x$ was ~0 or near 0 for large particles at the steepest experimental sites in all epochs, suggesting that our steepest site (S39) is near or at this critical gradient for large particles. In Spring 2021, $1/\mu_x$ was ~0 for medium particles, but in subsequent epochs the trend in $1/\mu_x$ suggest that S39 was just below this critical gradient for medium

565 particles.

Where data is present on the south-facing slope, A, B and μ_x values generally decrease between spring 2021 and spring 2022 (Fig. 11). This trend is clearly evident for larger particle sizes on steeper slopes, although it does not appear to hold for smaller particles on lower slopes. Many of these trends are also partially obscured by larger values in summer 2021 than in

570 the surrounding spring epochs, particularly for B and μ_x. Given the differences observed between summer and spring vegetation in the field, we assume this deviation reflects the effects of seasonal variation. We therefore exclude summer 2021 data from our consideration of post-fire recovery impacts and instead focus on differences between Spring 2021 and Spring 2022 on the south-facing study slope. We interpret the general decrease in tail heaviness (Fig. 11b-c), transport length scale (Fig. 11e-f) and mean travel distances (Fig. 11h-i) as consistent with the progressive recovery of vegetation after the

575 fire. This interpretation is supported by our estimated friction coefficients, which increased between Spring 2021 and Spring 2022 at all study sites on the SFS for all medium and large particles, reflecting the regrowth of vegetation (Fig. 13).

These findings align with differences in particle transport on burned and unburned slopes observed by previous studies demonstrating that travel distances become increasingly longer and heavy-tailed with decreasing surface roughness or increasing particle size or slope (Roth et al., 2020; Furbish et al., 2021b). However, a more nuanced assessment of the controls on particle transport may be derived from closer consideration of the cases that deviate from these expected trends. These cases appear to primarily reflect the influence of 1) seasonal or spatial variation in vegetation characteristics and 2) stochastic particle motion. Below, we discuss the effects of these factors on producing aspect-dependent particle behavior and the anomalous behavior of small particles on low slopes.

4.1.1 Small Particles and Stochastic Motion

Fig. 10d-10f shows that A values for small particles diverged and A values for medium and large particles converged near A=0 through time. We suggest that these changes were driven by size-dependent particle responses to the regrowth of vegetation. Small particles, which had a lower component of initial momentum than medium and large particles, were most sensitive to surface roughness (e.g., Gabet & Mendoza, 2012) and were more likely to experience a random component of motion upon impact with vegetation (Figs. 10d and 13d). We presume that this random motion and greater sensitivity to differences in vegetation structure between experimental sites caused values of A to diverge with time for small particles (Fig. 10d). We infer that the greater momentum of medium and large particles resulted in less random motion upon contact with vegetation, though particle momentum was still decreased [based on the observation that A began to converge around values closer to 0 over time (Figs. 10e and 10f)].

Our estimation of friction coefficient µ supports this interpretation, as µ was also sensitive to particle size and the smallest particles had the largest values of µ in all epochs. Stochasticity in µ also increased for smaller particles on lower slopes through time. For example, the decrease in µ for medium particles at S21 opposed the increase observed for most other medium particle groups, and µ diverged for all small particle groups at the SFS with time. (Fig. 13). These findings contrast interpretations made by Furbish et al. (2021b), who suggested that µ is insensitive to particle size for identical slope and roughness conditions. We suggest that µ may be insensitive to particle size when considering only roughness of the mineral surface (e.g., Gabet & Mendoza, 2012) or using larger rounded particles (e.g., Roth et al., 2020), but the presence of vegetation with spacing comparable to the range of experimental particle sizes results in size-selective values of µ.

4.1.2 Aspect-Dependent Differences in Particle Motion

The shift in travel distance distributions from Summer 2021 to Spring 2022 among large and medium particles is far less pronounced or even absent on the NFS (Fig. 9), especially among large particles where we see the largest shift on the SFS (Fig. 8). Without Spring 2021 data for the NFS, it is uncertain to what extent this difference is due to aspect-dependent variation in post-fire recovery or aspect-dependent seasonal variation in vegetation and soil moisture. However, our data and

field observations are consistent with the hypothesis that aspect-dependent differences between conditions on the NFS and SFS contributed to measurable differences in particle motion.

Aspect-dependency was more noticeable in Summer 2021 than Spring 2022, with greater differences in A, B, and mean travel distance for a given gradient and particle size between the NFS and SFS in Summer 2021 (Figs. 11b-c, 11e-f, and 11h-i). In Summer 2021, south-facing slopes above 26° also experienced uniformly higher mean travel distances than their north-facing counterparts (Fig. 11g-i). Between Summer 2021 and Spring 2022, friction coefficients on the SFS increased by an average 47% for all but two experimental particle size/slope groups. Over this same period, friction increased for only 5 of the 9 experimental groups on the NFS (average 50% increase), while 4 decreased by an average 12% (all large and one medium particle groups). These results indicate that the SFS: 1) experienced conditions in summer 2021 that were more conducive to long-distance particle motion overall, and 2) experienced conditions in Spring 2022 that disproportionately reduced particle motion relative to the NFS.

Though both the SFS and NFS exhibited some seasonal changes in vegetation (Figs. 5 & 6), the SFS experienced more extreme seasonal variation in both vegetation than the NFS due to the senescence and regrowth of dense seasonal grasses. In addition to simply adding new growth to the older, dried vegetation already present on the hillslope, healthy vegetation may have acted as a more effective barrier to the passage of particles in Spring 2022 than the dead vegetation in Summer 2021.

Other factors such as the coefficient of restitution of the mineral surface may also have evolved with seasonal changes in antecedent moisture. Based on field observations, soils on the SFS were more dry and less easily deformable than on the NFS during the summer. These observations are corroborated by measurements by Donaldson et al. (2024), who found that shallow soil moisture was generally lower on south-facing slopes in our study catchment. We suggest that the drier soils on the SFS may have increased the coefficient of restitution relative to the NFS. This would be expected to produce longer and more heavy-tailed particle travel distances on the SFS, consistent with our observations in Summer 2021.

4.1.3 Downslope Coarsening and Size Selective Transport

On the SFS, we observed nonlocal transport of medium and large particles at all sites with slopes of 26 degrees or greater in Spring 2021 (Figs. 8 & 10). At S26 and S39, a transition from nonlocal to local transport was observed between Spring 2021 and Summer 2021 for medium particles while large particles still experienced nonlocal transport. After Summer 2021, systematic changes in particle motion were not observable across all SFS experiments, but the maximum particle travel distance decreased for all SFS sites and all particle sizes. The post-fire observation of downslope coarsening along the SFS hillslope and the coarser particles found in the channel relative to the SFS hillslope (Fig. 7; Appendix A, Table A1) provide evidence of particle size-selective transport consistent with our experimental results. Previous field experiments and observations of post-fire dry ravel (DiBiase et al., 2017; DiBiase & Lamb 2017; Florsheim et al., 1991; Gabet, 2003; Lamb

et al., 2013; Roering & Gerber, 2005; Roth et al., 2020) report the sequestration of fine sediments by mineral or vegetative roughness as large particles bypass hillslope storage zones and are delivered to the channel network. This mechanism is interpreted to produce the variation between hillslope and channel particle size distributions shown in Fig. 7.

645

4.2 Implications for Post-fire Variability in Particle Fluxes

Although large particles were the most sensitive to slope, their sensitivity varied throughout the experimental epochs. A more nonlinear trend in A with slope in Summer 2021 (Fig. 11b) transitioned to a more linear trend in Spring 2022 (Fig. 11c). Our results suggest that immediately post-fire or in summer when vegetation strength is apparently reduced (e.g.,
650 Summer 2021 at our site), the aggregate travel distance distribution for all particle sizes naturally present would demonstrate a greater spread due to nonlinearity in large particle A values. Since the flux of dry ravel involves the convolution of the entrainment rate and R(x) (as described by Furbish et al., 2021a), this size-dependent nonlinearity in A values could contribute to the increased variance and nonlinearity in sediment fluxes commonly observed at high slopes (e.g., Roering et al., 1999). Evidence of nonlinear dependence of post-fire dry ravel flux has been previously presented by Gabet & Dunne
655 (2003) and ascribed to nonlocal transport (Gabet & Mendoza, 2012). In fact, we expect that entrainment rates may also vary with particle size and contribute to this nonlinearity, although further research is needed to constrain the relationship between particle sizes and biotically-driven entrainment rates.

4.3 Limitations and Outstanding Questions

Limitations of our work include a lack of control sites and no quantitative characterization of vegetation structures, which
660 should be considered in future data collection campaigns. We also suggest that future attempts at similar experiments would benefit from the collection of entrainment rate data.

In this study, we assume that our observations, particularly the transition from A>0 toward lower A values closer to 0 for M and L particles on the SFS, are caused by post-fire vegetation recovery. This interpretation is consistent with previous studies
665 demonstrating higher A values on smoother or burned sites relative to those on vegetated slopes (e.g., Furbish et al., 2021b; Roth et al., 2020). Future work would benefit from the inclusion of paired experiments at unburned control sites to better isolate the post-fire response relative to background transport characteristics. We emphasize the need for care in control site selection, however, as our data highlight the sensitivity of these experiments to not only macro-scale conditions (slope, aspect, vegetation), but microtopographic, biotic, and hydrologic conditions that may be subject to heterogeneity over both
670 experimental plot and catchment scales.

Another opportunity for future work complementary to the findings presented here would be the estimation of entrainment rates of ravel at the NFS and SFS. As the convolution of the entrainment rate and R(x) provides an estimate of flux (Furbish

et al., 2021a), deriving entrainment rates for the different particle sizes we used in our experiments would allow calculations of sediment flux due to dry ravel. Observations by others suggest that differences in soil cohesion associated with soil moisture and selective burrowing by California ground squirrels and Botta's pocket gophers may cause aspect dependency in the production and entrainment of ravel (e.g. Gabet, 2003; Ordeñana et al., 2012). Burrowing rodents apparently generate much of the mobile material at the mineral surface in the Arbor Creek Catchment (Fig. 1d, Image 1), and their presence likely influences hillslope morphology at the NFS and SFS. While the transport regime of medium and large particles was apparently similar at the NFS and SFS in Spring 2022, it would be useful to evaluate if the actual flux of ravel varied with aspect due to variable entrainment rates.

Previous studies have used descriptions of vegetation, such as roughness obtained from point cloud data to explore relationships between vegetation, slope, and particle transport (e.g., Roth et al., 2020). To characterize the mineral and vegetative components of surface roughness, we attempted to conduct structure-from-motion from images collected with drones in each experimental epoch, but the motion of dense grasses between image collections limited the quality of resulting point clouds. While point cloud data generally enables the calculation of useful topographic metrics such as roughness, the presence of dense vegetation inhibits the estimation of density at the mineral surface (e.g., Ashcroft et al., 2014; Grau et al., 2017). Physical vegetation sampling procedures are well established, including the point-centered quarter method (Dix, 1961), the frequency grid (Vogel & Masters, 2001), or alternative quadrat-based approaches (e.g., Knapp et al., 1986). We suggest that future studies of this nature utilize physical sampling procedures.

Finally, we emphasize uncertainty in the values of A presented for different experimental particle groups in this study. When considering these results, it is important to be aware that regressed A values generally represent an upper bound estimate of A due to potential overfitting of tails, which are generally the sparsest region in our empirical data. This issue is exemplified by the potential removal of the farthest travel distance recorded at S21 in Spring 2022 for small particles (Appendix B, Fig. B1), which would modify the R(x) distribution from one describing runaway motion (unrealistic at this site for small particles given our other results) to near uniform disentrainment. At some sites for which error was large relative to the calculated A value, it was difficult to distinguish clear signals in the transport regime from noise, which we assume was dominated by seasonal vegetation or resulted from under-sampling issues. Further experiments would be required to constrain the background level of travel distances at an unburned site or over longer time periods to validate whether this catchment had fully recovered by Spring 2022.

Conclusion

This study examines post-fire variability in rarified particle motion representative of dry ravel at Arbor Creek Catchment at Blue Oak Ranch Reserve in the Mt. Diablo Range of the California Bay Area. We conducted a series of particle drop

experiments using in situ particles in size classes representative of the range of particle sizes present at our field site, as measured by pebble counts along cross-slope transects. We fit our experimental particle travel distances to a Lomax distribution model for the travel distance exceedance probability of simulated ravel, in order to track the post-fire evolution of the form of these distributions with time, particle size, slope, and aspect. The Lomax parameter A, which describes the form of the travel distance exceedance distribution as light-tailed (bounded motion, local transport, A<0) exponential (isothermal, A=0) or heavy-tailed (runaway motion, nonlocal transport, A>0) was the primary metric used in our interpretations.

In considering different combinations of particle size, slope, and aspect through time, we identified that larger particles on steeper slopes in earlier experimental epochs were more likely to exhibit evidence of nonlocal transport. Our observations of size selective transport corresponded with evidence of downslope coarsening immediately after the fire, as determined from pebble counts along-slope and in the channel at the base of the hillslope. We also observed the transport regime of small particles (D_{50}=0.6 cm) on a south facing slope to diverge with time as vegetation recovered, while the behavior of medium (D_{50}=1.3 cm) and large (D_{50}=2.8 cm) particles became more similar across aspect and slope with time. Our results suggest that as vegetation recovered, the behavior of small particles became more dependent on site-specific vegetation structures and medium and large particles were less likely to exhibit evidence of runaway motion. Our estimated friction coefficients support our identification of vegetation dependent particle behavior, as the friction coefficient generally increased for medium and large particles as vegetation recovered on the south facing slope while trends for smaller particles on less steep slopes were inconsistent. For all particle sizes, the length scale of transport continued to decrease as vegetation recovered through the first two years post-fire, though seasonal changes to surface characteristics (vegetation, soil moisture) likely caused greater variability in transport behavior observed on south-facing aspects relative to north-facing aspects through time.

Appendix A: Experimental particle and site parameters

Table A1: Hillslope particle size statistics. Median, minimum, maximum, standard deviation and number of measurements from pebble counts on cross-slope transects along the study hillslope during each epoch. Numbered transect positions describe the downslope distance from Site S21, and Channel (S) denotes the channel at the base of the south-facing slope. In Spring 2021, measurements at 0 and 20 m were recorded with 1 mm precision, measurements at 50 m were recorded with 5 mm precision. In Summer 2021 and Spring 2022 measurements were recorded with 0.01 mm precision.

Transect position (m)	Epoch	Intermediate diameter (cm)				N particles
		Median	Min.	Max.	Std. dev.	
0	SP 21	0.6	0.3	3.0	0.4	111
	SU 21	0.593	0.066	2.371	0.411	111
	SP 22	0.575	0.236	2.312	0.418	102
10	SP 21	--				
	SU 21	0.55	0.01	2.611	0.428	111
	SP 22	0.678	0.255	3.550	0.470	100
20	SP 21	0.7	0.3	2.0	0.3	100
	SU 21	0.740	0.010	4.883	0.713	109
	SP 22	0.670	0.269	2.160	0.403	100
30	SP 21	--				
	SU 21	0.547	0.010	3.09	0.467	111
	SP 22	0.673	0.276	2.348	0.365	100
40	SP 21	--				
	SU 21	0.523	0.010	3.016	0.468	110
	SP 22	0.759	0.222	2.333	0.438	100
50	SP 21	--	0.5	3.5	--	91
	SU 21	0.717	0.118	4.194	0.767	121
	SP 22	0.703	0.323	3.198	0.460	100
Channel (S)	SP 21	--				
	SU 21	1.951	0.268	8.827	1.206	150
	SP 22	0.925	0.292	3.843	0.683	100

Table A2: Median, minimum, maximum, and standard deviation of particle sizes for all experimental particle classes. Particle minimum and maximum values are reported as bin edges for Spring 2021 due to measurement imprecision, and as measured sample minimum and maximum for summer 2021 and Spring 2022, during which pre-collected and painted particles were used.

Epoch	Site	Particle size class	Intermediate diameter (cm)				N
			Median	Min. (≥)	Max. (<)	Std. Dev.	
Spring 2021	S21*	Small	--	0.25	0.75	--	68-214
	S26	Medium	--	0.75	2.25	--	41-230
	S39	Large	--	2.25	3.25	--	42-58
Summer 2021 Spring 2022	all sites	Small	0.63	0.33	0.95	0.11	89-199
		Medium	1.31	0.97	1.72	0.16	93-200
		Large	2.80	2.27	3.14	0.18	97-204

*No particles in large size class dropped at site S21, Spring 2021

Table A3: Censor distances for all sites. Site S30 was censored in Summer 2021 only, Site N33 was censored in Spring 2022 only, and Site S39 was censored in all three epochs. The variable censor point at S39 caused by the variable distance to the sloping channel at the base of the site required manual censorship based on drop position.

Site	S21	S26	N26	S30	N30	N33	S39
Censor Distance (m)	None	None	None	10.5	None	7.5	6.2-8.6

Table A4: Comparison of Lomax parameter A resulting from alternative division of medium (M) and large (L) particle classes for relevant experiments conducted in Spring 2021. The classification of several particles recorded as 1.75 cm (i.e., falling between 1.5 and 2 cm) and 2 cm (1.75 - 2.25 cm) in diameter was particularly sensitive to our selection of the binning threshold between medium and large size classes. We tested thresholds of 1.75 and 2.25 cm for comparison, and found that a boundary of 2.25 cm resulted in less severe under sampling of the medium class at S39 without meaningfully altering results for the large particle class. We also note the that the lower edge of the Spring 2021 medium bin (0.75 cm) falls below the medium size range in the later epochs

(0.97 cm). Given these considerations, we selected the 2.25 cm threshold for all analyses presented in the main text.

M/L Bound	S21 M	S26 M	S26 L	S39 M	S39 L
A value with L ≥ 1.75 cm	-0.19	0.20	0.21	0.07	1.98
A value with L ≥ 2.25 cm	-0.17	0.26	0.25	1.03	2.26

Table B1: Summary of number of experimental particles (N), A values, standard error of A (σA), B values (m), and standard error of B [σB (m)]. Red text indicates sites at which σA is greater than |A|, indicating substantial uncertainty in the sign of A.

Site	Epoch	Particle Size														
		S					M					L				
		N	A	σA	B	σB	N	A	σA	B	σB	N	A	σA	B	σB
S21	Sp '21	79	0.03	±0.08	0.03	±0.00	46	-0.17	±0.06	0.05	±0.00	--				
	Su '21	201	-0.23	±0.06	0.07	±0.01	204	-0.06	±0.07	0.07	±0.01	204	-0.04	±0.08	0.09	±0.01
	Sp '22	100	0.42	±0.12	0.01	±0.00	100	-0.15	±0.06	0.04	±0.00	100	-0.09	±0.07	0.07	±0.01
S26	Sp '21	226	0.06	±0.09	0.04	±0.01	240	0.26	±0.10	0.07	±0.01	58	0.25	±0.10	0.16	±0.02
	Su '21	200	-0.22	±0.06	0.09	±0.01	200	-0.18	±0.06	0.10	±0.01	200	0.01	±0.08	0.11	±0.01
	Sp '22	100	-0.47	±0.04	0.06	±0.00	100	-0.10	±0.07	0.04	±0.00	100	0.10	±0.09	0.08	±0.01
S30	Sp '21	--														
	Su '21	201	0.14	±0.09	0.10	±0.02	200	0.43	±0.12	0.18	±0.03	201	0.11	±0.09	1.80	±0.21
	Sp '22	100	-0.02	±0.08	0.05	±0.01	100	-0.07	±0.07	0.10	±0.01	100	0.35	±0.12	0.37	±0.05
S39	Sp '21	83	-0.14	±0.06	0.07	±0.01	82	1.03	±0.18	0.09	±0.02	42	2.27	±0.52	1.03	±0.28
	Su '21	100	0.12	±0.09	0.21	±0.03	100	-0.06	±0.07	0.57	±0.06	100	1.83	±0.39	1.04	±0.26
	Sp '22	100	0.11	±0.09	0.09	±0.01	100	0.07	±0.09	0.29	±0.04	100	0.58	±0.15	0.69	±0.12
N26	Sp '21	--														
	Su '21	100	-0.01	±0.08	0.08	±0.01	100	-0.11	±0.07	0.11	±0.01	100	-0.06	±0.07	0.17	±0.02
	Sp '22	100	-0.24	±0.06	0.05	±0.00	100	-0.01	±0.08	0.05	±0.01	100	0.12	±0.09	0.16	±0.02
N30	Sp '21	--														
	Su '21	106	0.23	±0.10	0.06	±0.01	110	-0.20	±0.06	0.22	±0.02	101	-0.12	±0.07	0.44	±0.04
	Sp '22	100	-0.02	±0.08	0.06	±0.01	100	0.22	±0.10	0.09	±0.01	100	0.28	±0.10	0.25	±0.04
N33	Sp '21	--														
	Su '21	105	0.14	±0.09	0.11	±0.02	112	-0.05	±0.07	0.23	±0.03	100	0.42	±0.12	0.56	±0.09
	Sp '22	100	-0.16	±0.06	0.08	±0.01	100	0.16	±0.10	0.10	±0.01	100	0.49	±0.13	0.46	±0.08

S21: R(x) vs. Distance (m)
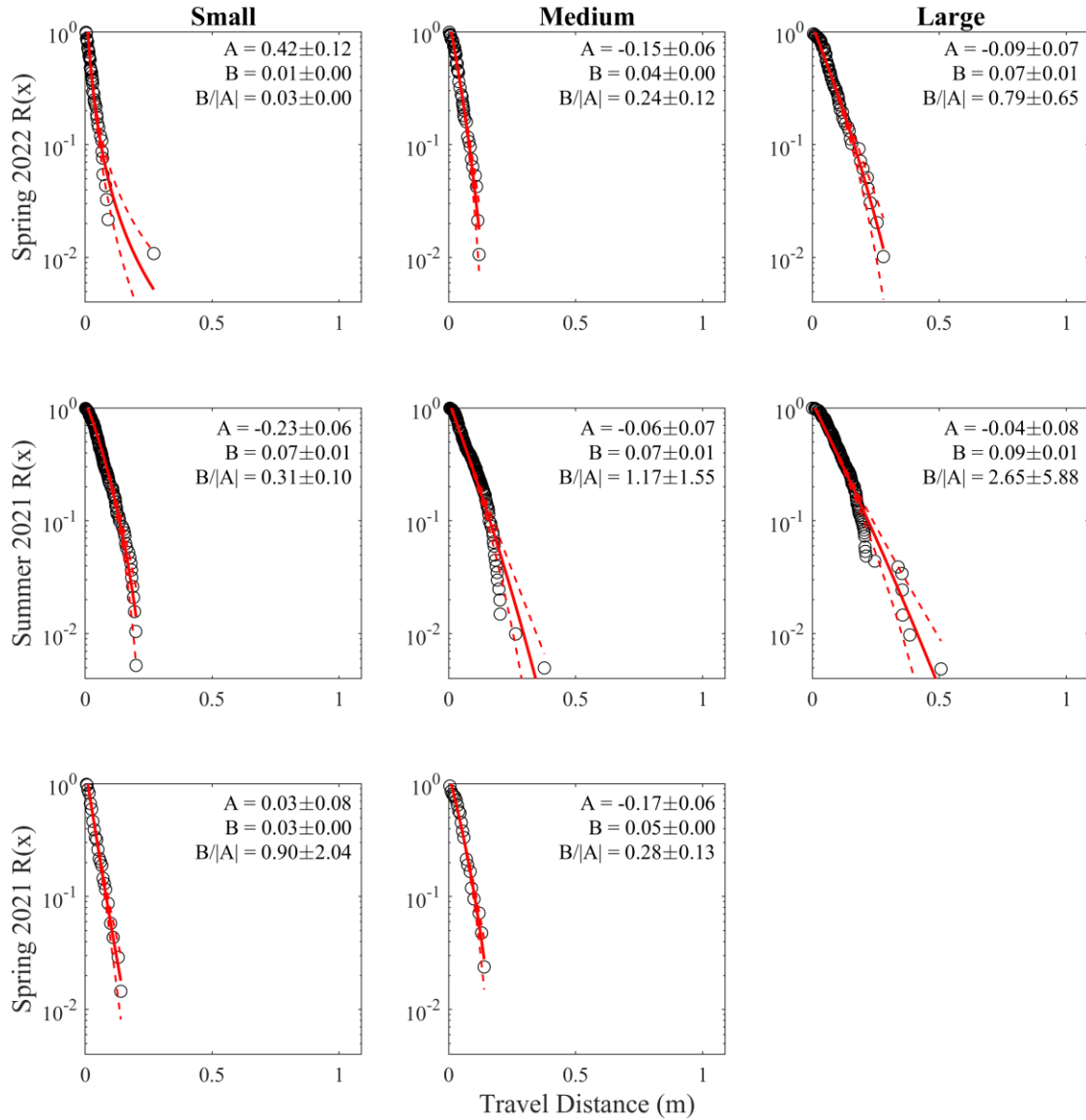
Figure B1: Empirical R(x) and modeled R(xi) for site S21 annotated with Lomax parameters A and B and characteristic distance B/|A|. Error estimations are denoted with parameter values. Black circles are empirical data. Dashed red lines represent variability in R(x) with the standard error in A.
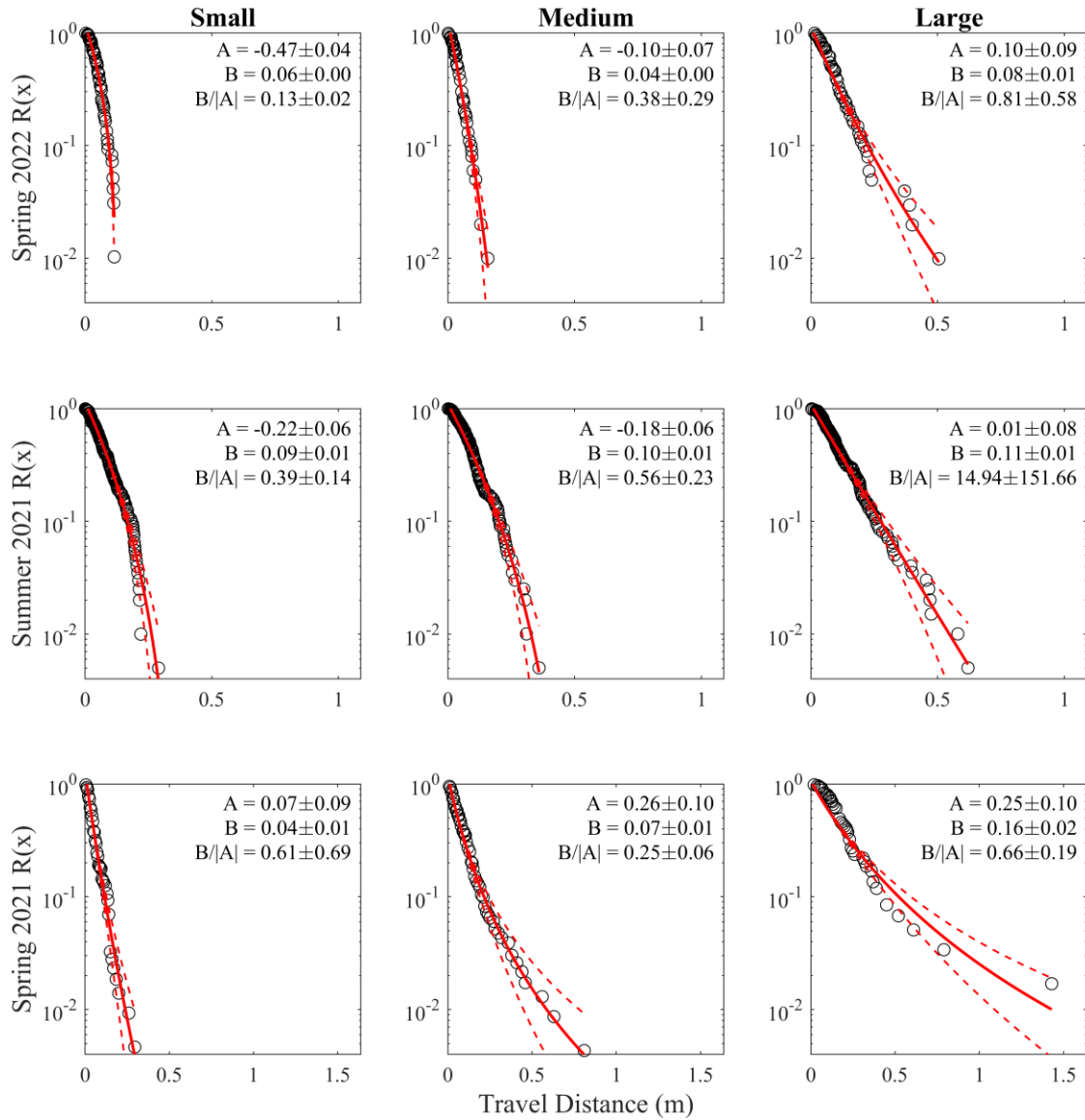
765 **Figure B2: Empirical R(x) and modeled R(xi) for site S26 annotated with Lomax parameters A and B and characteristic distance B/|A|. Error estimations are denoted with parameter values. Black circles are empirical data. Dashed red lines represent variability in R(x) with the standard error in A.**
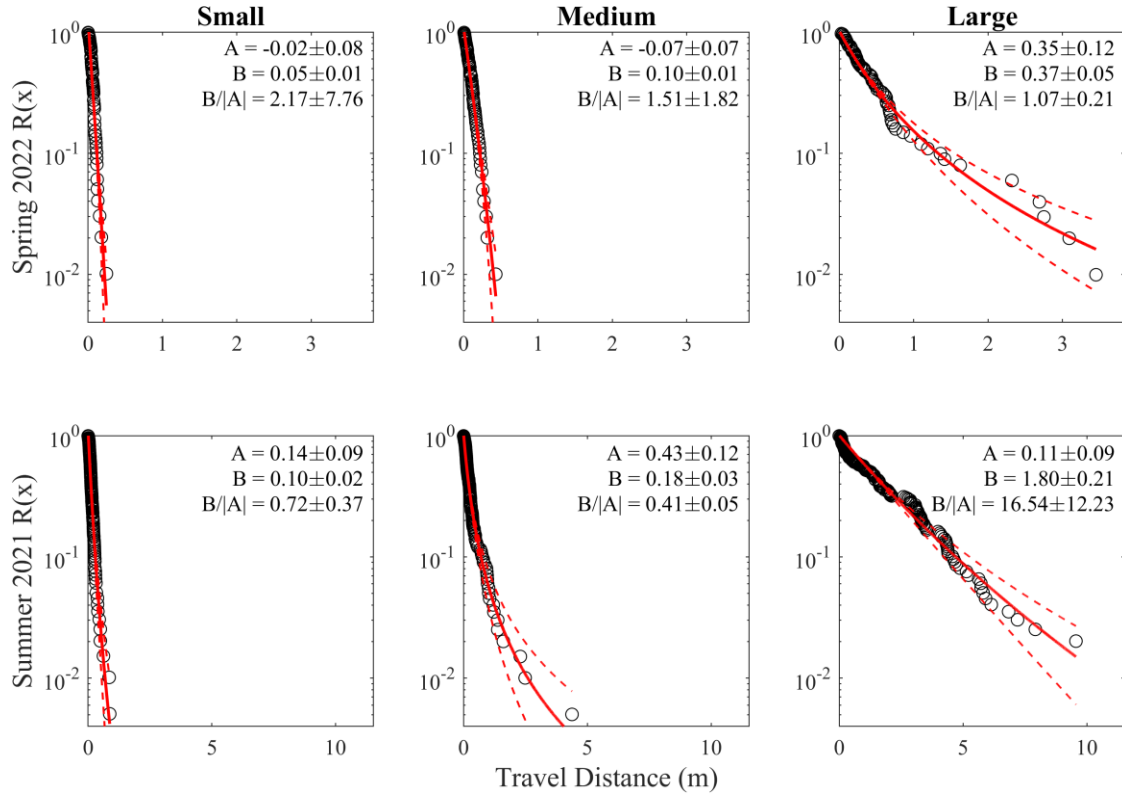
Figure B3: Empirical R(x) and modeled R(xi) for site S30 annotated with Lomax parameters A and B and characteristic distance B/|A|. Error estimations are denoted with parameter values. Black circles are empirical data. Dashed red lines represent variability in R(x) with the standard error in A.

S39: R(x) vs. Distance (m)
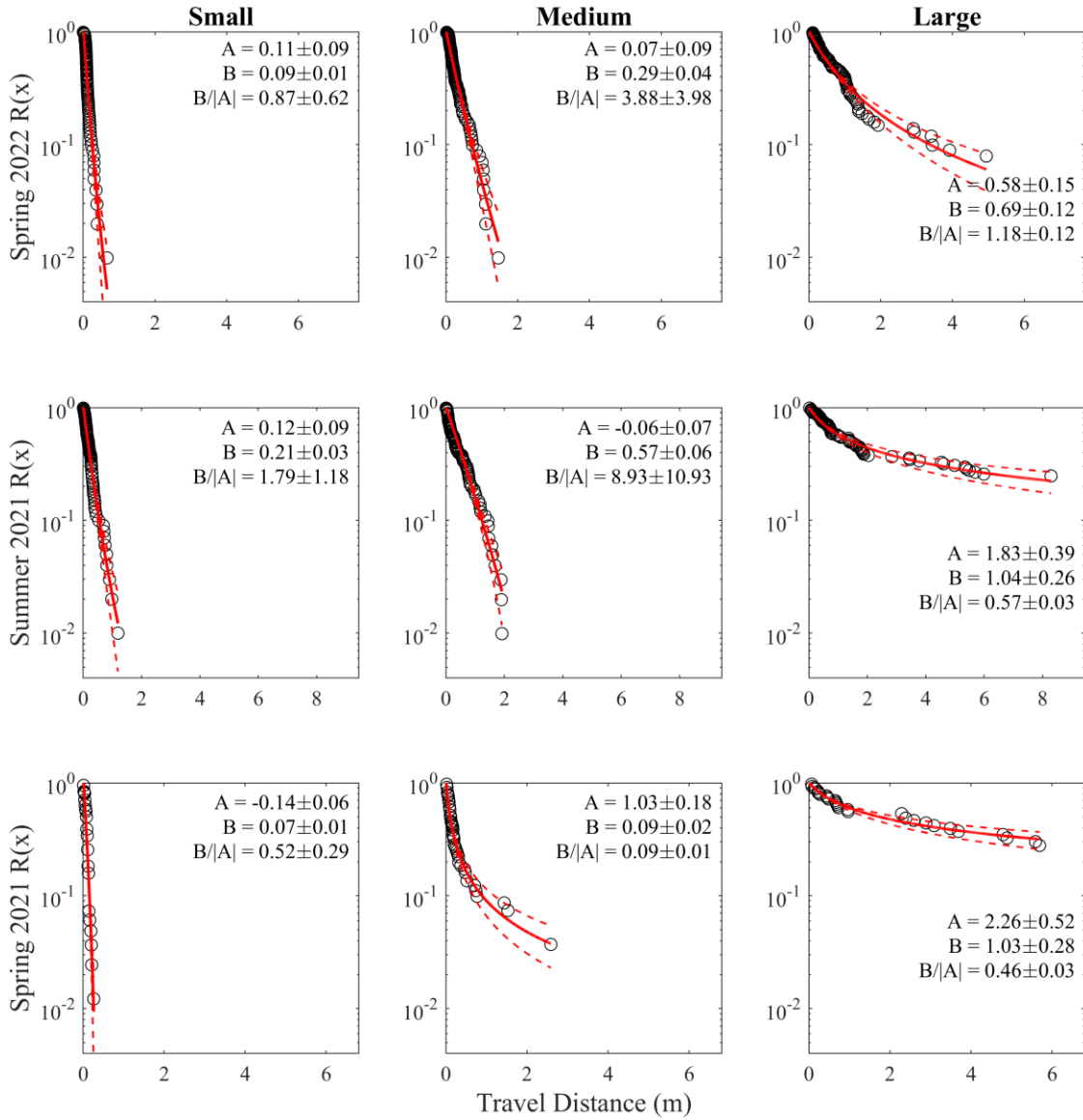
Figure B4: Empirical R(x) and modeled R(xi) for site S39 annotated with Lomax parameters A and B and characteristic distance B/|A|. Error estimations are denoted with parameter values. Black circles are empirical data. Dashed red lines represent variability in R(x) with the standard error in A.

N26: R(x) vs. Distance (m)
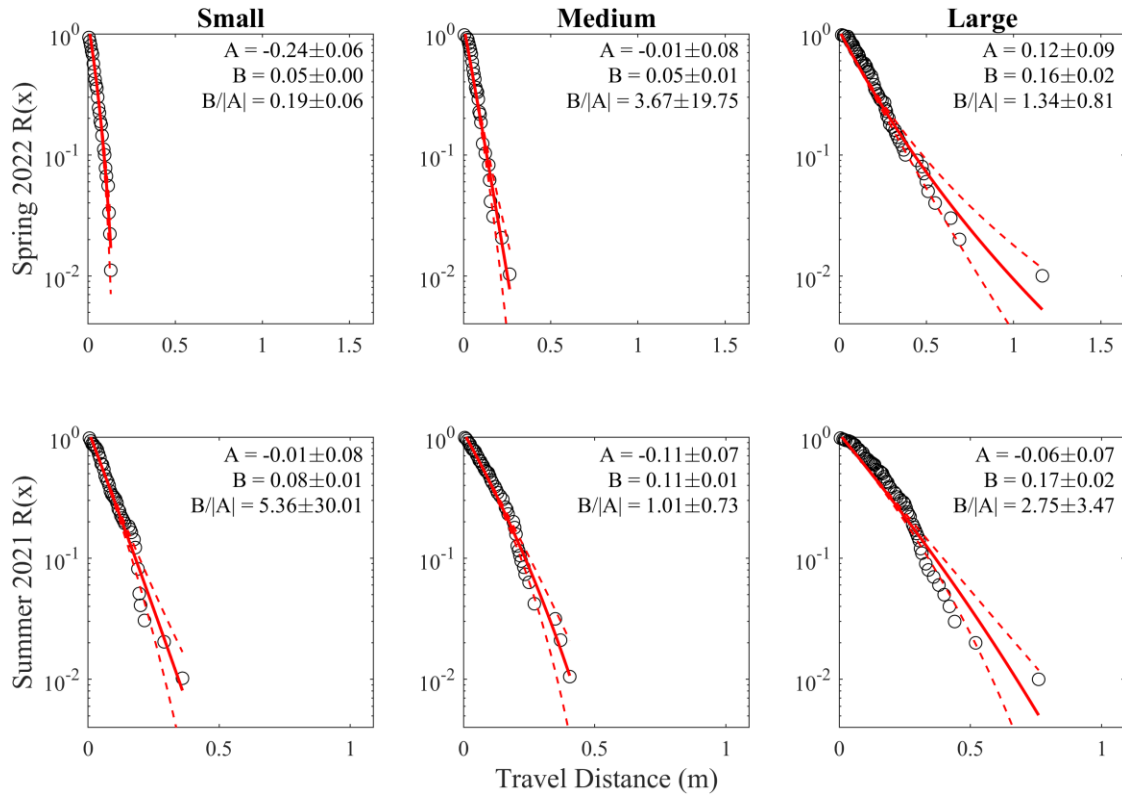
785 **Figure B5: Empirical R(x) and modeled R(xi) for site N26 annotated with Lomax parameters A and B and characteristic distance B/|A|. Error estimations are denoted with parameter values. Black circles are empirical data. Dashed red lines represent variability in R(x) with the standard error in A.**

790

N30: R(x) vs. Distance (m)
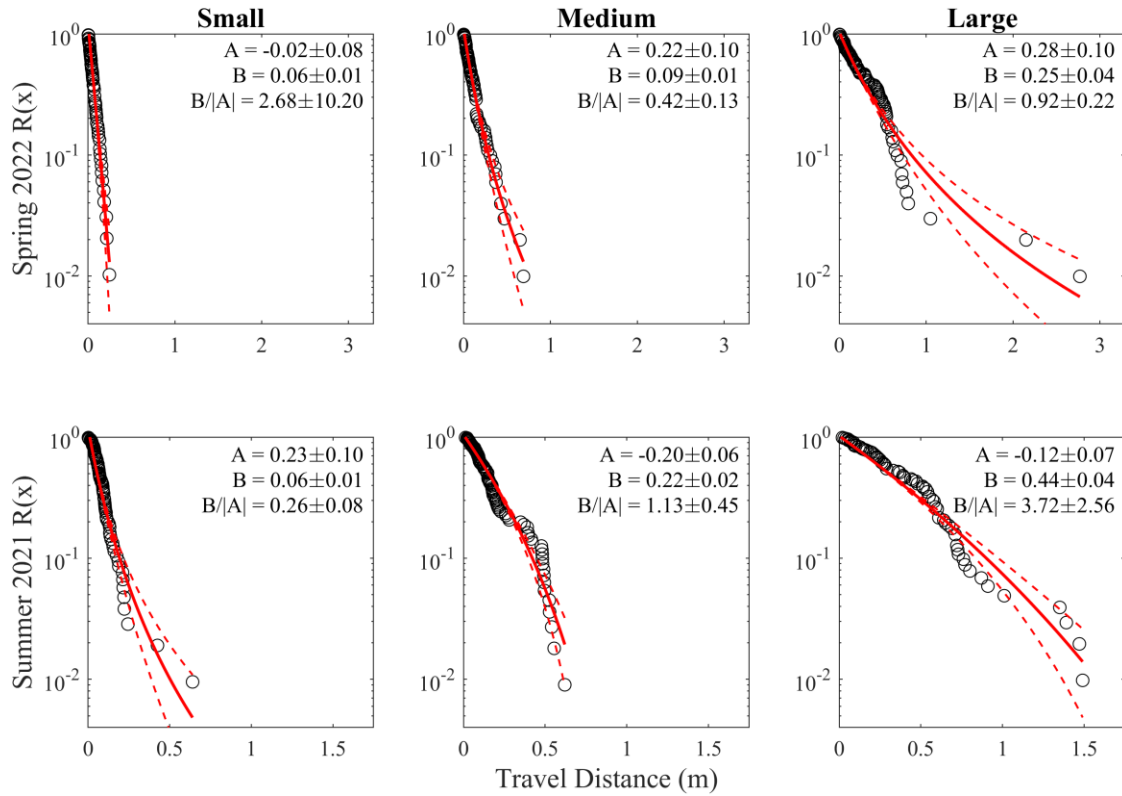
Figure B6: Empirical R(x) and modeled R(xi) for site N30 annotated with Lomax parameters A and B and characteristic distance B/|A|. Error estimations are denoted with parameter values. Black circles are empirical data. Dashed red lines represent variability in R(x) with the standard error in A.

795

N33: R(x) vs. Distance (m)
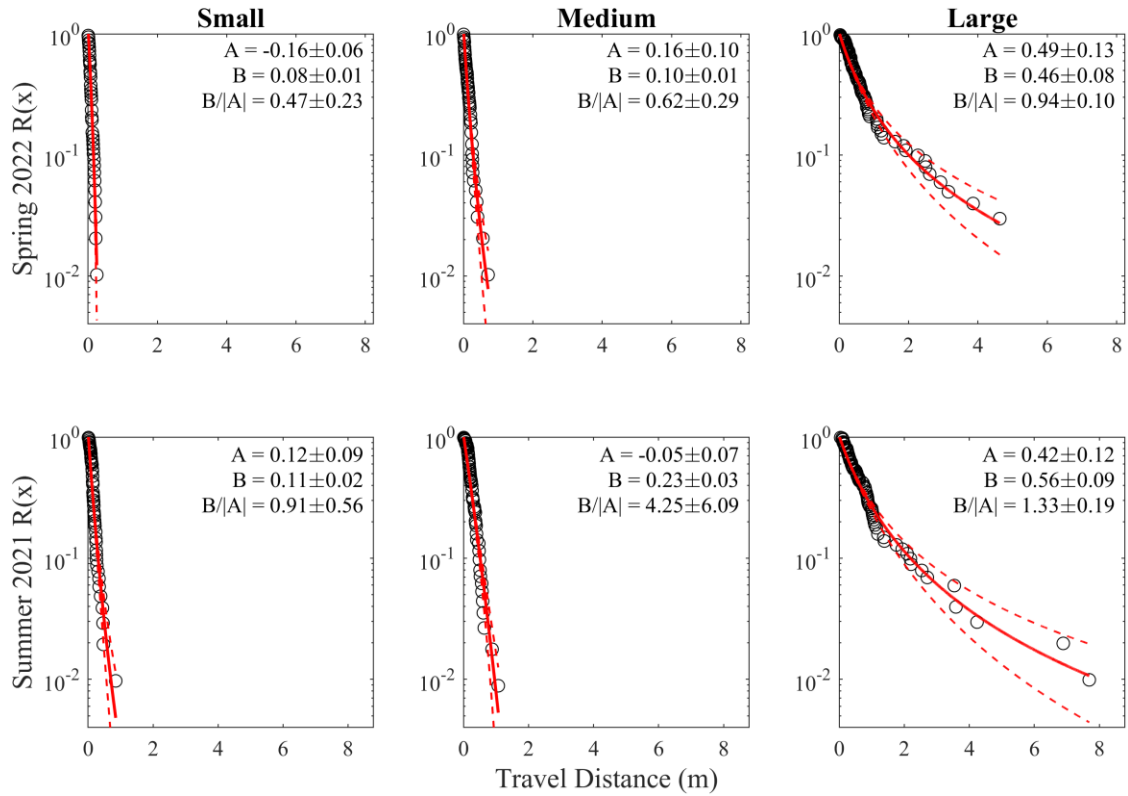
Figure B7: Empirical R(x) and modeled R(xi) for site N33 annotated with Lomax parameters A and B and characteristic distance B/|A|. Error estimations are denoted with parameter values. Black circles are empirical data. Dashed red lines represent variability in R(x) with the standard error in A.

800
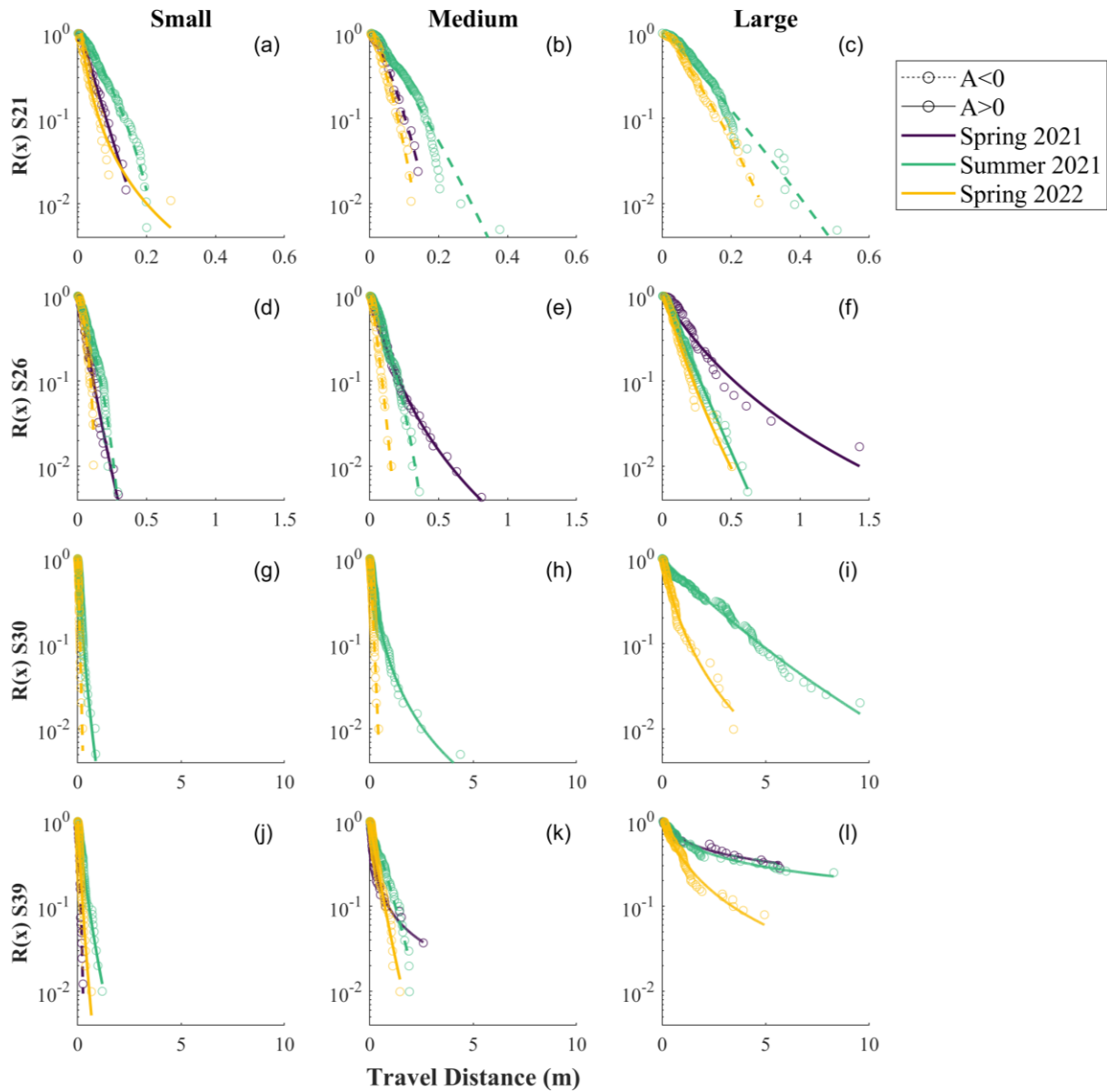
Figure B8: Empirical and modeled travel distance exceedance distributions R(x) for all SFS sites with equal scaling of the horizontal axes for each site. Dashed lines indicate models with A<0 (bounded motion) and solid lines indicate models with A>0 (runaway motion). Open circles represent empirical data. Columns correspond to particle sizes (small, medium, large) while rows indicate experimental site.
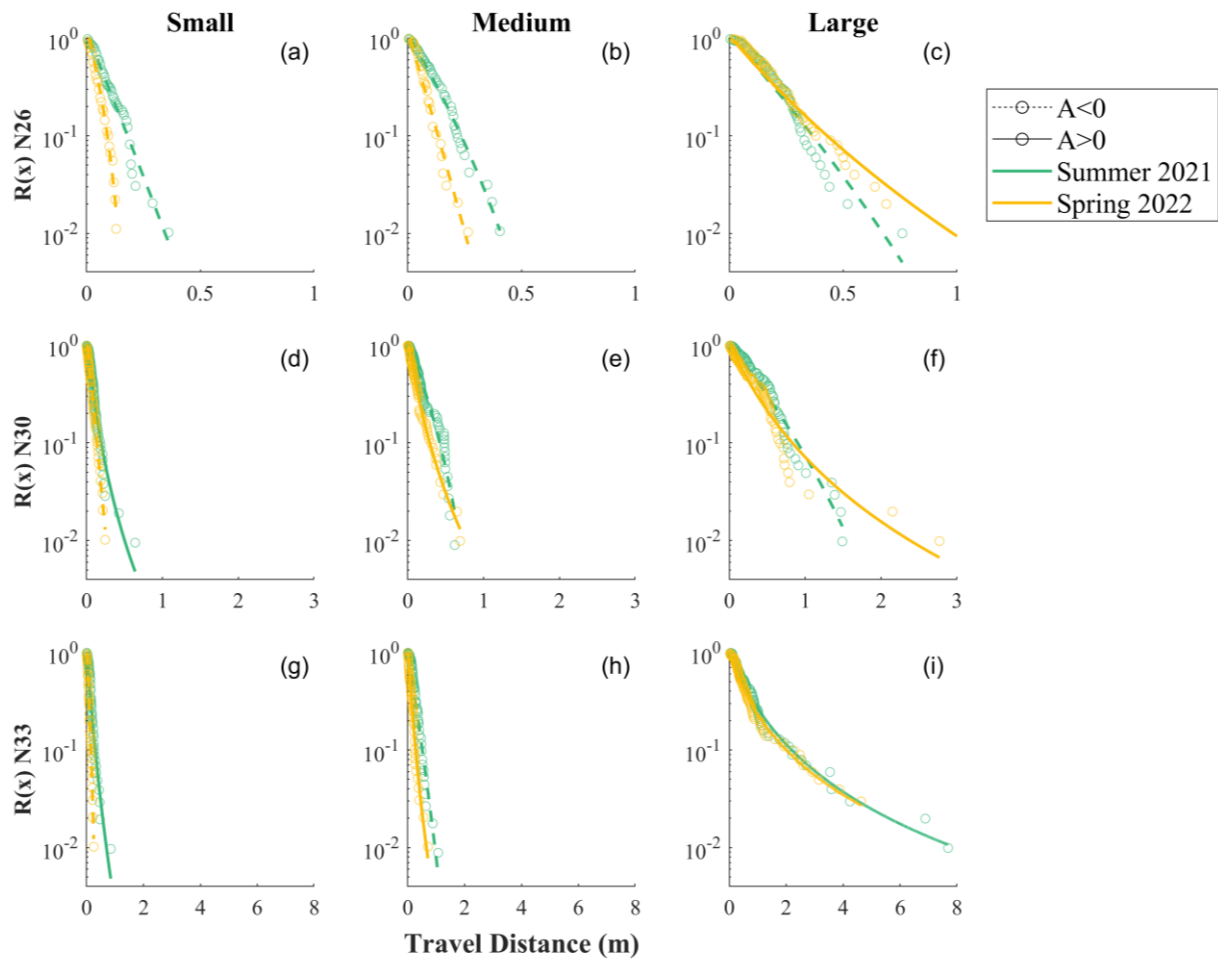
Figure B9: Empirical and modeled travel distance exceedance distributions R(x) for all SFS sites with equal scaling of the horizontal axes for each site. Dashed lines indicate models with A<0 (bounded motion) and solid lines indicate models with A>0 (runaway motion). Open circles represent empirical data. Columns correspond to particle sizes (small, medium, large) while rows indicate experimental site.

Appendix C: Additional visualizations of trends in A, B, 1/μₓ, and μ
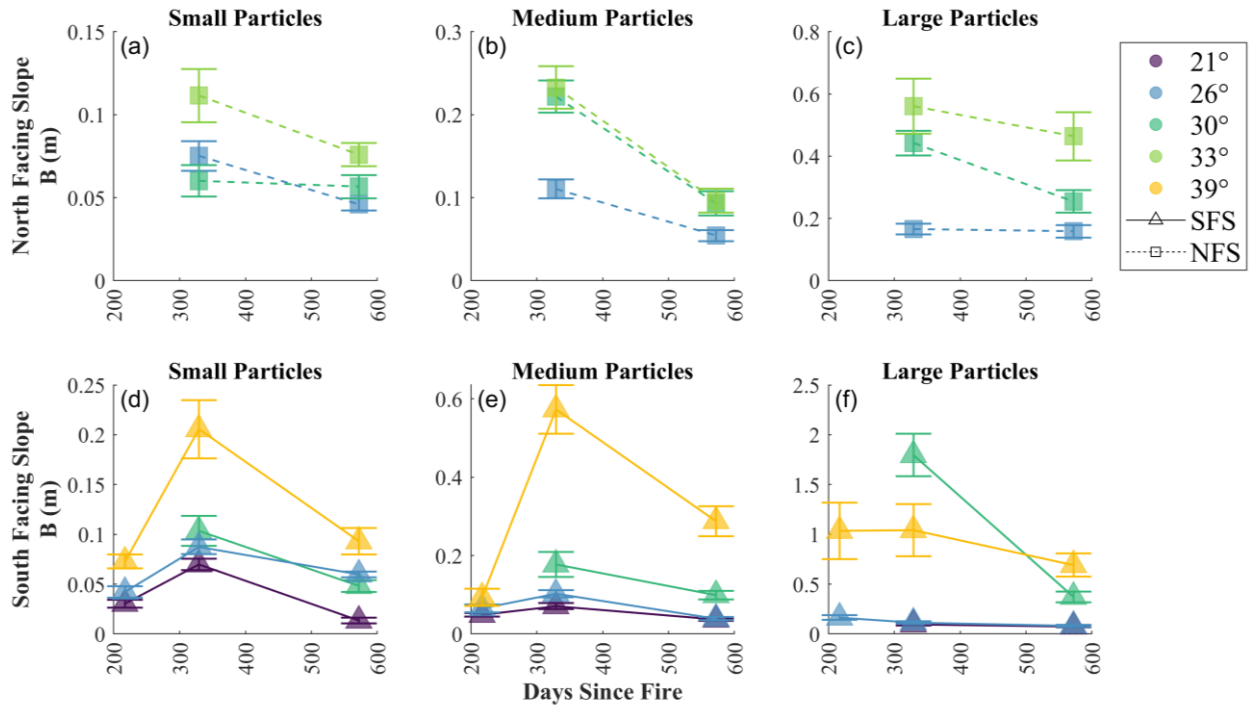
Figure C1: Values of Lomax scale parameter B (m) for all combinations of particle size class, slope angle (°), experimental epoch, and aspect. Error bars represent standard error ($\pm\sigma_B$) of B obtained from bootstrapping. Field visits occurred 217, 329, and 572 days post-fire.
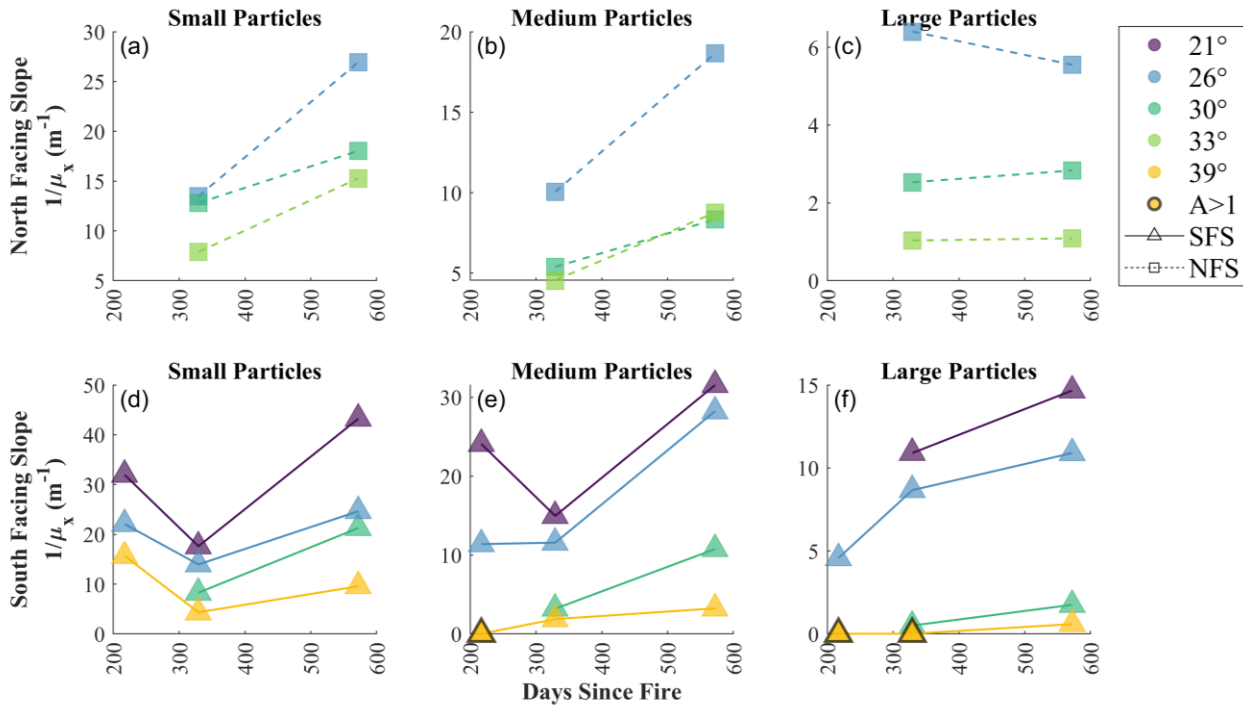
825

Figure C2: Values of the reciprocal of mean travel distance ($1/\mu_x$) (m^{-1}) for all combinations of particle size class, slope angle (°), experimental epoch, and aspect. Undefined values of $1/\mu_x$ where A>1 are represented by filled black markers and plotted at a value of 0 (medium and large particles at S39 in Spring 2021 and large particles at S39 in Summer 2021). Field visits occurred 217, 329, and 572 days post-fire.

830
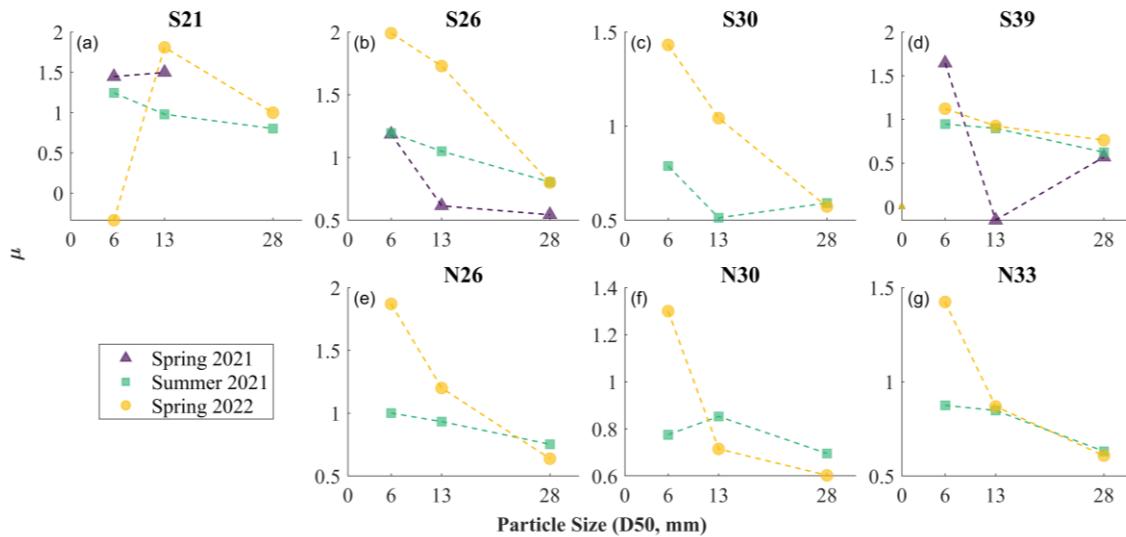
Figure C3: Trends in the coefficient of friction (μ) with particle size for each experimental site and epoch. Subplot titles designate aspect (S = south facing slope, N = north facing slope) and slope in degrees (e.g., S21 has a slope of 21 degrees).
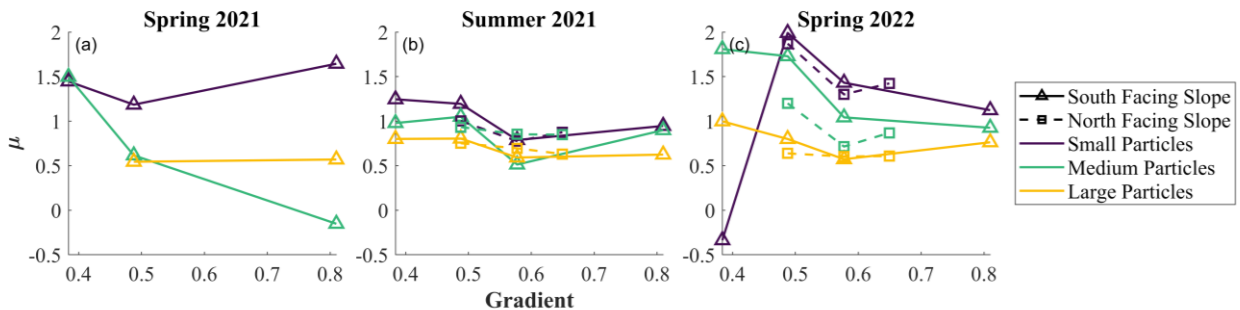
Figure C4: Trends in the coefficient of friction (μ) with hillslope gradient for each experimental epoch.

Code and Data Availability

The V1.0.0 version of the code (Lomax2) and data (particle travel distances, pebble counts) required to recreate the analyses presented in this manuscript can be found on Github and are archived with Zenodo (Jacobson, 2023). Topographic data are available in the UNAVCO online data archive at https://doi.org/10.7283/cp79-v370

Author Contributions

Conceptualization, D.L.R., M.Z., K.J.; Methodology, H.L.J., D.L.R., G.W.; Software, H.L.J., D.L.R.; Formal analysis, H.L.J., D.L.R., G.W.; Investigation, H.L.J., D.L.R., M.Z.; Data curation, H.L.J.; Writing – Original Draft, H.L.J.; Writing –

Review & Editing, H.L.J., D.L.R., G.W., M.Z., K.J.; Visualization, H.L.J.; Supervision, D.L.R., G.W.; Funding Acquisition, D.L.R., M.Z., K.J.

Competing interests

The authors declare that they have no conflict of interest.

850 **Acknowledgements**

This work was supported with National Science Foundation (NSF) Division of Earth Sciences award no. 2123220. The authors thank Zac Harlow and Zac Tuthill for assisting with site access and providing equipment at Blue Oak Ranch Reserve (DOI: 10.21973/N3ZT08), part of the University of California Natural Reserve System. We greatly appreciate Amanda Donaldson, Lauren Giggy, Michael Wilshire, Nerissa Barling, and Dylan Elliott, members of the UC Santa Cruz Watershed
855 Hydrology Laboratory, and Mel Zhang, Natalie Lasater, Stephen Gialamas, and Samantha Burton, members of the Surface Processes and Geomorphology Group at CSM, for assisting with field work and data management. Lidar acquisition services were provided by the GAGE Facility, operated by UNAVCO, Inc., with support from the National Science Foundation, the National Aeronautics and Space Administration, and the U.S. Geological Survey under NSF Cooperative Agreement EAR-1724794. We appreciate the comments on this manuscript by Jonathan Perkins, and thank Emmanuel Gabet and an
860 anonymous reviewer for their peer reviews.

References

Ashcroft, M. B., Gollan, J. R., and Ramp, D.: Creating vegetation density profiles for a diverse range of ecological habitats using terrestrial laser scanning, Methods in Ecology and Evolution, 5, 263–272, https://doi.org/10.1111/2041-210X.12157, 2014.
865 Bennett, K. A.: Effects of slash burning on surface soil erosion rates in the Oregon Coast Range, M.S. Thesis, Oregon State University, 1982.
Black, T. A. and Montgomery, D. R.: Sediment transport by burrowing mammals, Marin County, California, Earth Surf. Proc. Land. 16, 163–172, https://doi.org/10.1002/esp.3290160207, 1991.
Bunte, K.: Sampling surface and subsurface particle-size distributions in wadable gravel-and cobble-bed streams for analyses
870 in sediment transport, hydraulics, and streambed monitoring. US Department of Agriculture, Forest Service, Rocky Mountain Research Station, http://dx.doi.org/10.2737/RMRS-GTR-74, 2001.

Collins, L. and Ketcham, B.: Fluvial Geomorphic Response Of a Northern California Coastal Stream To Wildfire, Lessons Learned From the October 1995 Fire, US Department of the Interior, National Park Service, Point Reyes National Seashore, 59-79, 2001.

875   Dibblee, T. W., and Minch, J. A. Geologic map of the Mount Day quadrangle, Santa Clara & Alameda Counties, California. Dibblee Geological Foundation, Dibblee Foundation Map DF-236, 2006.

DiBiase, R. A. and Lamb, M. P.: Vegetation and wildfire controls on sediment yield in bedrock landscapes, Geophys. Res. Lett., 40, 1093–1097, https://doi.org/10.1002/grl.50277, 2013.

DiBiase, R. A. and Lamb, M. P.: Dry sediment loading of headwater channels fuels post-wildfire debris flows in bedrock

880   landscapes, Geology, 48, 189–193, https://doi.org/10.1130/G46847.1, 2019.

DiBiase, R. A., Lamb, M. P., Ganti, V., and Booth, A. M.: Slope, grain size, and roughness controls on dry sediment transport and storage on steep hillslopes, J. Geophys. Res.-Earth, 122, 941–960, https://doi.org/10.1002/2016JF003970, 2017.

Dix, R. L.: An Application of the Point-Centered Quarter Method to the Sampling of Grassland Vegetation, Rangeland

885   Ecology & Management/Journal of Range Management Archives ,14, 2, 63-69, https://doi.org/10.2307/3894717, 1961.

Donaldson, A., Dralle, D., Barling, N., Callahan, R. P., Loik, M. E., and Zimmer, M.: Aspect Differences in Vegetation Type Drive Higher Evapotranspiration on a Pole-Facing Slope in a California Oak Savanna, J. Geophys. Res-Biogeo, 129, e2024JG008054, https://doi.org/10.1029/2024JG008054, 2024.

Donaldson, A. M., Zimmer, M., Huang, M.-H., Johnson, K. N., Hudson-Rasmussen, B., Finnegan, N., Barling, N., and

890   Callahan, R. P.: Symmetry in Hillslope Steepness and Saprolite Thickness Between Hillslopes With Opposing Aspects, J. Geophys. Res.-Earth, 128, e2023JF007076, https://doi.org/10.1029/2023JF007076, 2023.

East, A. E., Logan, J. B., Dartnell, P., Lieber-Kotz, O., Cavagnaro, D. B., McCoy, S. W., and Lindsay, D. N.: Watershed Sediment Yield Following the 2018 Carr Fire, Whiskeytown National Recreation Area, Northern California, Earth and Space Science, 8, e2021EA001828, https://doi.org/10.1029/2021EA001828, 2021.

895   Fitch, H.S.: Ecology of the California ground squirrel on grazing lands, The American Midland Naturalist, 39, 513–596, https://www.jstor.org/stable/2421524, 1948.

Florsheim, J. L., Keller, E. A., and Best, D. W.: Fluvial sediment transport in response to moderate storm flows following chaparral wildfire, Ventura County, southern California, GSA Bulletin, 103, 504–511, https://doi.org/10.1130/0016-7606(1991)103<0504:FSTIRT>2.3.CO;2, 1991.

900   Foufoula-Georgiou, E., Ganti, V., and Dietrich, W. E.: A nonlocal theory of sediment transport on hillslopes, J. Geophys. Res.-Earth, 115, https://doi.org/10.1029/2009JF001280, 2010.

Furbish, D. J. and Haff, P. K.: From divots to swales: Hillslope sediment transport across divers length scales, J. Geophys. Res.-Earth, 115, https://doi.org/10.1029/2009JF001576, 2010.

Furbish, D. J. and Roering, J. J.: Sediment disentrainment and the concept of local versus nonlocal transport on hillslopes, J.

905   Geophys. Res.-Earth, 118, 937–952, https://doi.org/10.1002/jgrf.20071, 2013.

Furbish, D. J., Roering, J. J., Doane, T. H., Roth, D. L., Williams, S. G. W., and Abbott, A. M.: Rarefied particle motions on hillslopes: 1. Theory, Physical: Earth Surf. Dynam., 9, 539-576 https://doi.org/10.5194/esurf-9-539-2021, 2021a.

Furbish, D. J., Williams, S. G. W., Roth, D. L., Doane, T. H., and Roering, J. J.: Rarefied particle motions on hillslopes – Part 2: Analysis, Earth Surf. Dynam., 9, 577–613, https://doi.org/10.5194/esurf-9-577-2021, 2021b.

910 Gabet, E. J.: Sediment transport by dry ravel, J. Geophys. Res.-Sol. Ea., 108, https://doi.org/10.1029/2001JB001686, 2003.

Gabet, E. J. and Dunne, T.: A stochastic sediment delivery model for a steep Mediterranean landscape, Water Resour. Res., 39, https://doi.org/10.1029/2003WR002341, 2003.

Gabet, E. J. and Mendoza, M. K.: Particle transport over rough hillslope surfaces by dry ravel: Experiments and simulations with implications for nonlocal sediment flux, J. Geophys. Res.-Earth, 117, https://doi.org/10.1029/2011JF002229, 2012.

915 Grau, E., Durrieu, S., Fournier, R., Gastellu-Etchegorry, J.-P., and Yin, T.: Estimation of 3D vegetation density with Terrestrial Laser Scanning data using voxels. A sensitivity analysis of influencing parameters, Proc. SPIE, 191, 373–388, https://doi.org/10.1016/j.rse.2017.01.032, 2017.

Guilinger, J. J., Gray, A. B., Barth, N. C., and Fong, B. T.: The Evolution of Sediment Sources Over a Sequence of Postfire Sediment-Laden Flows Revealed Through Repeat High-Resolution Change Detection, J. Geophys. Res.-Earth, 125,
920 e2020JF005527, https://doi.org/10.1029/2020JF005527, 2020.

Hey, R. D. and Thorne, C. R.: Accuracy of Surface Samples from Gravel Bed Material, J. Hydraul. Eng., 109, 842–851, https://doi.org/10.1061/(ASCE)0733-9429(1983)109:6(842), 1983.

Jackson, M. and Roering, J. J.: Post-fire geomorphic response in steep, forested landscapes: Oregon Coast Range, USA, Quaternary Sci. Rev., 28, 1131–1146, https://doi.org/10.1016/j.quascirev.2008.05.003, 2009.

925 Jacobson, H.: Lomax2, Zenodo [code]. https://zenodo.org/doi/10.5281/zenodo.10048973, 2023.

Kean, J. W., Staley, D. M., and Cannon, S. H.: In situ measurements of post-fire debris flows in southern California: Comparisons of the timing and magnitude of 24 debris-flow events with rainfall and soil moisture conditions, J. Geophys. Res.-Earth, 116, https://doi.org/10.1029/2011JF002005, 2011.

Kley, N. J and Kearney, M.: Chapter 17. Adaptations for Digging and Burrowing, in: Fins into Limbs: Evolution,
930 Development, and Transformation, edited by Hall, B. K., University of Chicago Press, Chicago, 284-309, https://doi.org/10.7208/9780226313405-018, 2006.

Knapp, A. K. and Hulbert, L. C.: Production, Density and Height of Flower Stalks of Three Grasses in Annually Burned and Unburned Eastern Kansas Tallgrass Prairie: A Four Year Record, The Southwestern Naturalist, 31, 235–241, https://doi.org/10.2307/3670564, 1986.

935 Lagarias, J. C., Reeds, J. A., Wright, M. H., Wright, P. E.: Convergence Properties of the Nelder-Mead Simplex Method in Low Dimensions. SIAM J. Optimiz., 9, 112-147, https://doi.org/10.1137/S1052623496303470, 1998.

Lamb, M. P., Scheingross, J. S., Amidon, W. H., Swanson, E., and Limaye, A.: A model for fire-induced sediment yield by dry ravel in steep landscapes, J. Geophys. Res.-Earth, 116, https://doi.org/10.1029/2010JF001878, 2011.

Lamb, M. P., Levina, M., DiBiase, R. A., and Fuller, B. M.: Sediment storage by vegetation in steep bedrock landscapes: Theory, experiments, and implications for postfire sediment yield, J. Geophys. Res.-Earth, 118, 1147–1160, https://doi.org/10.1002/jgrf.20058, 2013.

Lavé, J. and Burbank, D.: Denudation processes and rates in the Transverse Ranges, southern California: Erosional response of a transitional landscape to external and anthropogenic forcing, J. Geophys. Res.-Earth, 109, https://doi.org/10.1029/2003JF000023, 2004.

Mataix-Solera, J., Cerdà, A., Arcenegui, V., Jordán, A. and Zavala, L.M.: Fire effects on soil aggregation: a review. Earth-Science Reviews, 109, 1-2, 44-60, https://doi.org/10.1016/j.earscirev.2011.08.002, 2011.

Milojević, S.: Power law distributions in information science: Making the case for logarithmic binning, J. Am. Soc. Inf. Sci. Tec., 61, 2417–2425, https://doi.org/10.1002/asi.21426, 2010.

Ordeñana, M. A., Van Vuren, D. H., and Draper, J. P.: Habitat associations of California ground squirrels and Botta's pocket gophers on levees in California, J. Wildlife Manage., 76, 1712–1717, https://doi.org/10.1002/jwmg.402, 2012.

Parks, S. A. and Abatzoglou, J. T.: Warmer and Drier Fire Seasons Contribute to Increases in Area Burned at High Severity in Western US Forests From 1985 to 2017, Geophysical Res. Lett., 47, https://doi.org/10.1029/2020GL089858, 2020.

Parsons, A., Robichaud, P.R., Lewis, S.A., Napper, C. and Clark, J.T.: Field guide for mapping post-fire soil burn severity (Vol. 243), US Department of Agriculture, Forest Service, Rocky Mountain Research Station, 2010.

Perkins, J. P., Diaz, C., Corbett, S. C., Cerovski-Darriau, C., Stock, J. D., Prancevic, J. P., Micheli, E., and Jasperse, J.: Multi-Stage Soil-Hydraulic Recovery and Limited Ravel Accumulations Following the 2017 Nuns and Tubbs Wildfires in Northern California, J. Geophys. Res.-Earth, 127, https://doi.org/10.1029/2022JF006591, 2022.

Reed, S., and Amundson, R.: Sediment, gophers, and time: a model for the origin and persistence of Mima mound—vernal pool topography in the Great Central Valley. Vernal Pool Landscapes, 14, 15-27, S2CID 28512602, 2007.

Roering, J. J. and Gerber, M.: Fire and the evolution of steep, soil-mantled landscapes, Geology, 33, 349–352, https://doi.org/10.1130/G21260.1, 2005.

Roering, J. J., Kirchner, J. W., and Dietrich, W. E.: Evidence for nonlinear, diffusive sediment transport on hillslopes and implications for landscape morphology, Water Resour. Res., 35, 853–870, https://doi.org/10.1029/1998WR900090, 1999.

Roth, D. L., Doane, T. H., Roering, J. J., Furbish, D. J., and Zettler-Mann, A.: Particle motion on burned and vegetated hillslopes, Proc. Natl. Acad. Sci. U.S.A., 117, 25335–25343, https://doi.org/10.1073/pnas.1922495117, 2020.

Samson, L., Ippolito, I., Bideau, D., and Batrouni, G.G.: Motions of grains down a bumpy surface, Chaos, 9, 639-648, https://doi.org/10.1063/1.166437, 1999.

Shakesby, R. A. and Doerr, S. H.: Wildfire as a hydrological and geomorphological agent, Earth-Sci. Rev., 74, 269–307, https://doi.org/10.1016/j.earscirev.2005.10.006, 2006.

Sorensen, D. C., and Moré, J. C.: Computing a Trust Region Step. SIAM J. Sci. Stat. Comp., 4, 553–572, https://doi.org/10.1137/0904038, 1983.

Swanson, F. J.: Fire and geomorphic process, Fire Regime and Ecosystem Properties, 26, 401–421, 1981.

Tucker, G. E. and Bradley, D. N.: Trouble with diffusion: Reassessing hillslope erosion laws with a particle-based model, J. Geophys. Res.-Earth, 115, https://doi.org/10.1029/2009JF001264, 2010.

975 Vogel, K. P. and Masters, R. A.: Frequency grid—a simple tool for measuring grassland establishment, J. Range Manage., 54, 6, 635-655, https://doi.org/10.2307/4003666, 2001.

Wells, W. G.: The effects of fire on the generation of debris flows in southern California, Reviews in Engineering Geology, 7, 105-114, https://doi.org/10.1130/REG7-p105, 1987.

Wohl, E. E., Anthony, D. J., Madsen, S. W., and Thompson, D. M.: A comparison of surface sampling methods for coarse
980 fluvial sediments, Water Resources Research, 32, 3219–3226, https://doi.org/10.1029/96WR01527, 1996.

Wondzell, S. M. and King, J. G.: Postfire erosional processes in the Pacific Northwest and Rocky Mountain regions, Forest Ecol. and Manag., 178, 75–87, https://doi.org/10.1016/S0378-1127(03)00054-9, 2003.